The impact of multi-species surface chemical observations assimilation on the air quality forecasts in China

Zhen Peng[1*], Lili Lei[1, 2], Zhiquan Liu[3*], Jianning Sun[1, 4], Aijun Ding[1, 4], Junmei Ban[3],

Dan Chen[5], Xingxia Kou[5], Kekuan Chu[1,2]

1 School of Atmospheric Sciences, Nanjing University, Nanjing, China

2 Key Laboratory of Mesoscale Severe Weather/Ministry of Education, Nanjing University, Nanjing, China

3 National Center for Atmospheric Research, Boulder, Colorado, USA

4 Jiangsu Provincial Collaborative Innovation Center for Climate Change, Nanjing, China

5 Institute of Urban Meteorology, CMA, Beijing, China

Abstract. An Ensemble Kalman Filter data assimilation (DA) system has been developed to improve air quality forecasts using surface measurements of PM_{10}, $PM_{2.5}$, SO_2, NO_2, O_3 and CO together with an online regional chemical transport model, WRF-Chem (Weather Research and Forecasting with Chemistry). This DA system was applied to simultaneously adjust the chemical initial conditions (ICs) and emission inputs of the species affecting PM_{10}, $PM_{2.5}$, SO_2, NO_2, O_3 and CO concentrations during an extreme haze episode that occurred in early October 2014 over the East Asia. Numerical experimental results indicate that ICs play key roles in $PM_{2.5}$, PM_{10} and CO forecasts during the severe haze episode over the North China Plain. The 72-h verification forecasts with the optimized ICs and emissions performed very similarly to the verification forecasts with only optimized ICs and the prescribed emissions. For the first-day forecast, near perfect verification forecasts results were achieved. However, with longer range forecasts, the DA impacts decayed quickly. For the SO_2 verification forecasts, it was efficient to improve the SO_2 forecast via the joint adjustment of SO_2 ICs and emissions. Large improvements were achieved for SO_2 forecasts with both the optimized ICs and emissions for the whole 72-h forecast range. Similar improvements were achieved for SO_2 forecasts with optimized ICs only for just the first 3 h, and then

30   the impact of the ICs decayed quickly. For the NO_2 verification forecasts, both forecasts

31   performed much worse than the control run without DA. Plus, the 72-h O_3 verification

32   forecasts performed worse than the control run during the daytime, due to the worse

33   performance of the NO_2 forecasts, even though they performed better at night. However,

34   relatively favorable NO_2 and O_3 forecast results were achieved for the Yangtze River

35   delta and Pearl River delta regions.

37   **1 Introduction**

38   Predicting and simulating air quality remains a challenge in heavily polluted regions

39   (Wang et al., 2014; Ding et al. 2016). Chemical data assimilation (DA), which

40   combines observations and model simulations, is recognized as one effective method

41   to improve air quality forecasts. It has been widely used to assimilate aerosol

42   measurements from both ground-based and space-borne platforms, including surface

43   PM_{10} observations (Jiang et al., 2013; Pagowski et al., 2014), surface $PM_{2.5}$

44   observations (Li et al., 2013; Zhang, 2016), Lidar observations (Yumimoto et al., 2007,

45   2008), aerosol optical depth products from AERONET (the AErosol RObotic

46   NETwork) (Schutgens et al., 2010a-b, 2012), and from various satellites (Sekiyama et

47   al., 2010; Liu et al., 2011; Dai et al., 2014). These studies indicate that assimilating

48   observations can substantially improve the spatiotemporal variations of aerosol in the

49   simulation and forecasts.

50   Aerosols are not only primarily emitted, but also with a larger portion secondary

51   formed through reactions with several gaseous-phases precursors and oxidants in the

52   atmosphere (Huang et al., 2014; Nie et al., 2014; Xie et al., 2015). So, observations of

53   trace gases are also useful in assimilating data for aerosol simulations and forecasts.

54   Efforts to assimilate atmospheric-composition observations, like O_3, SO_2, NO, NO_2,

55   CO, and NH_3, have also been made. For example, Elbern et al. (1997, 1999, 2000, 2001,

56   2007) developed a 4D-VAR (four-dimensional variational) system to assimilate surface

57   measurements of O_3, SO_2, NO and NO_2 to improve air quality forecasts with the joint

58   adjustment of initial conditions (ICs) and emission rates. Later, van Loon et al. (2000)

59   assimilated O_3 in the transport chemistry model LOTOS, based on an Ensemble Kalman

Filter (EnKF). Heemink and Segers (2002) attempted to reconstruct NO_x and volatile organic compound (VOC) emissions for O_3 forecasting by assimilating O_3. Carmichael et al. (2003, 2008a, 2008b) developed 4D-VAR and EnKF systems to assimilate O_3 and NO_2 to improve ICs and emission sources for O_3 forecasting. Hakami et al. (2005) constrained black carbon (BC) emissions during the Asian Pacific Regional Aerosol Characterization Experiment. Henze et al. (2007, 2009) estimated SO_x, NO_x and NH_3 emissions based on a 4D-VAR method by assimilating surface sulfate and nitrate aerosol observations. Other studies have estimated the NO_x (van der et al., 2006, 2017; Mijling et al., 2009, 2012, 2013; Ding. et al., 2015) and SO_2 emissions (van der et al., 2017) based on an extended Kalman filter by assimilating SO_2 and NO_2 retrievals from SCIAMACHY (SCanning Imaging Absorption spectroMeter for Atmospheric CHartographY) and OMI (Ozone Monitoring Instrument). Barbu et al. (2009) applied an EnKF to optimize the emissions and conversion rates using surface measurements of SO_2 and sulfate. McLinden (2016) constrained SO_2 emissions using space-based observations.

In recent years, severe haze pollution episodes have begun to occur more frequently in China, especially in the megacity clusters of eastern China (e.g., Parrish and Zhu, 2009; Sun et al., 2015; Zhang et al., 2015a). Thus, regional haze, especially when accompanied by extremely high $PM_{2.5}$ concentrations, has drawn significant research interest. However, there are large uncertainties involved in the numerical prediction of atmospheric aerosols. During severe haze pollution episodes, air quality models often underestimate the extreme peak mass concentration of particulate matter (Wang et al., 2014). Previous studies have revealed that the assimilation of atmospheric-composition observations can improve air quality forecasts by constraining the uncertainties of both the chemical ICs and emissions (Tang et al., 2010, 2011, 2013, 2016; Miyazaki et al., 2012, 2013, 2014). Peng et al. (2017) demonstrated that significant improvements in forecasting $PM_{2.5}$ can be achieved via the joint adjustment of ICs and source emissions using an EnKF to assimilate surface $PM_{2.5}$ observations.

In 2013, China launched an atmospheric environmental monitoring system that provides real-time and online atmospheric chemical observations, including PM_{10},

90 PM2.5, SO2, NO2, O3, and CO (http://113.108.142.147:20035/emcpublish/). This

91 dataset provides an opportunity to improve air quality forecasts using DA. However,

92 such fruitful observations are less used in air quality forecast despite of large

93 discrepancy existed between the forecast and observations. But it is now possible to

94 estimate the impact on forecast improvement of simultaneously assimilating various

95 surface observations. Thus, we developed an EnKF system that can simultaneously

96 assimilate surface measurements of PM_{10}, PM2.5, SO2, NO2, O3 and CO to correct WRF-

97 Chem (Weather Research and Forecasting model with Chemistry) forecasts using the

98 Goddard Chemistry Aerosol Radiation and Transport (GOCART) aerosol scheme. As

99 an extension to Peng et al. (2017), the impact of simultaneously assimilating various

100 surface aerosol and chemical observations was investigated.

101 Sections 2 and 3 briefly describe the DA system and observations used in this

102 study, respectively. The experimental design is introduced in Section 4. Finally, the

103 assimilation results are presented in Section 5, before a brief summary in Section 6.

104

2 DA system

106 The DA system in this study was the same as the one used in Peng et al. (2017). It

107 can simultaneously analyze the chemical ICs and emissions with the assimilation of

108 surface PM2.5 observations. A brief summary of the DA system is introduced here.

109 In every DA cycle, the ensemble emission scaling factors $\boldsymbol{\lambda}^\mathrm{f}$ are first calculated

110 by the forecast model of scaling factors $\mathbf{M}_\mathrm{SF}$ (see details of $\mathbf{M}_\mathrm{SF}$ in section 2.2). Then,

111 the ensemble forecast emissions $\mathbf{E}^\mathrm{f}$ are calculated using the following equation:

$$\mathbf{E}_{i,t} = \boldsymbol{\lambda}_{i,t}\mathbf{E}_t^\mathrm{p}, (i = 1, \dots, N), \tag{1}$$

113 where $\mathbf{E}_t^\mathrm{p}$ is the prescribed anthropogenic emission. The ensemble members of

114 chemical fields $\mathbf{C}^\mathrm{f}$ are forecasted using WRF-Chem, forced by the forecast emissions

115 $\mathbf{E}^\mathrm{f}$ whose ICs are previously analyzed concentration fields. Now, the background of

116 the joint vector, $\mathbf{x}^\mathrm{f} = \left[\mathbf{C}^\mathrm{f}, \boldsymbol{\lambda}^\mathrm{f}\right]^\mathrm{T}$, has been produced. Then, the analyzed state vector,

117 $\mathbf{x}^\mathrm{a} = [\mathbf{C}^\mathrm{a}, \boldsymbol{\lambda}^\mathrm{a}]^\mathrm{T}$, is optimized using an ensemble square root filter (EnSRF). Finally, the

118 assimilated emissions $\mathbf{E}^\mathrm{a}$ can be obtained using equation (1). It is noted that the

119 optimized emissions are only the results of a mathematical optimum by utilizing

120 observations. If the optimized emissions used in the EnSRF experiment run with pure

121 concentrations as state vectors are identical to the emissions obtained from the joint

122 EnSRF experiment run with concentrations and emission factors (representing

123 emissions) as state vectors, identical results may be obtained.

124

2.1 WRF-Chem model

126 The model used to simulate the transport of aerosols and chemical species was the

127 WRF-Chem (Grell et al., 2005). As in Peng et al. (2017), we used version 3.6.1 and the

128 physical and chemical parameterization options are listed in Table 1. The model

129 computational domain covered almost the whole China and the horizontal resolution

130 was 40.5 km. Figure 1b shows our area of interest, the North China Plain (NCP). The

131 model included 57 vertical levels and the model top was 10 hPa.

132   The hourly prior anthropogenic emissions were based on the Multi-resolution

133 Emission Inventory for China (MEIC) (Li et al., 2014) for October 2010, instead of the

134 regional emission inventory in Asia (Zhang et al., 2009) for the year 2006 in Peng et al.

135 (2017). The reason we chose the MEIC-2010 was that the total emissions are reasonable

136 for cities over the NCP (Zheng et al., 2016). The original resolution of the MEIC-2010

137 is $0.25° \times 0.25°$, but has been processed to match the model resolution (40.5 km) (Chen

138 et al., 2016). No time variation was added to maintain objectivity in the prior

139 anthropogenic emissions.

140

2.2 Forecast model of scaling factors

142 In this work, the primary sources to be optimized were the emissions of PM_{10}, $PM_{2.5}$,

143 SO_2, NO, NH_3 and CO. The sources of NH_3 were analyzed because they also impact

144 greatly on the aerosols distribution. Thus, the emission scaling factors $\lambda_{i,t}^f =$

145 ($\lambda_{PM2.5}^f, \lambda_{PM10}^f, \lambda_{SO2}^f, \lambda_{NO}^f, \lambda_{NH3}^f, \lambda_{CO}^f$) were prepared by the forecast model of scaling

146 operator $\mathbf{M}_{SF}$ before WRF-Chem integration.

147   We used the same persistence forecast operator $\mathbf{M}_{SF}$ to forecast $\lambda_{i,t}^f$ as in Peng

148   et al. (2017). The forecast operator was developed by using the ensemble forecast

149   chemical fields. Thus,

150
$$\kappa_{i,t} = \frac{\mathbf{C}^{\mathrm{f}}_{i,t}}{\overline{\mathbf{C}^{\mathrm{f}}_t}}, (i = 1, \dots, N), \tag{2}$$

151
$$(\kappa_{i,t})_{\mathrm{inf}} = \beta(\kappa_{i,t} - \overline{\kappa_t}) + \overline{\kappa_t}, (i = 1, \dots, N), \tag{3}$$

152
$$\lambda^{\mathrm{p}}_{i,t} = (\kappa_{i,t})_{\mathrm{inf}}, \tag{4}$$

153
$$\lambda^{\mathrm{f}}_{i,t} = \frac{1}{4}(\lambda^{\mathrm{a}}_{i,t-3} + \lambda^{\mathrm{a}}_{i,t-2} + \lambda^{\mathrm{a}}_{i,t-1} + \lambda^{\mathrm{p}}_{i,t}), (i = 1, \dots, N), \tag{5}$$

154   where $\mathbf{C}^{\mathrm{f}}_{i,t}$ is the ith ensemble member of the chemical fields at time t, and

155    $\overline{\mathbf{C}^{\mathrm{f}}_t} = \frac{1}{N}\sum_{i=1}^{N}\mathbf{C}^{\mathrm{f}}_{i,t}$ is the ensemble mean; $\kappa_{i,t}$ is the ensemble concentration ratios and

156    $\overline{\kappa_t}$ is the ensemble mean of $\kappa_{i,t}$ with values of 1; β is the inflation factor to keep the

157   ensemble spreads of $\kappa_{i,t}$ at a certain level; $\lambda^{\mathrm{a}}_{i,t-1}$, $\lambda^{\mathrm{a}}_{i,t-2}$ and $\lambda^{\mathrm{a}}_{i,t-3}$ are the previous

158   assimilated emission scaling factors. It is noted that $\lambda^{\mathrm{f}}_{i,t}$ are spatially varying because

159   they are calculated by using the spatially varying variables, the forecast chemical fields

160    $\mathbf{C}^{\mathrm{f}}_{i,t}$. Besides, There are very few negative values for $(\kappa_{i,t})_{\mathrm{inf}}$ after inflation. A quality

161   control procedure is performed for $(\kappa_{i,t})_{\mathrm{inf}}$ before further appliance. All these

162   negative data were set as 0 in this work. Then $(\kappa_{i,t})_{\mathrm{inf}}$ were re-centered to ensure the

163   ensemble mean values of $(\kappa_{i,t})_{\mathrm{inf}}$ were all 1. Besides, another quality control

164   procedure is performed for $\lambda^{\mathrm{a}}_{i,t}$ to keep them positive. Thus, all $\lambda^{\mathrm{f}}_{i,t}$ and $\lambda^{\mathrm{a}}_{i,t}$ could

165   be positive.

166   In this study, the ensemble forecast chemical fields of PM_{25}, PM_{10}, SO_2, NO, NH_3

167   and CO of the previous assimilation cycle are respectively used to calculate the

168   emission scaling factors ($\lambda^{\mathrm{f}}_{\mathrm{PM2.5}}, \lambda^{\mathrm{f}}_{\mathrm{PM10}}, \lambda^{\mathrm{f}}_{\mathrm{SO2}}, \lambda^{\mathrm{f}}_{\mathrm{NO}}, \lambda^{\mathrm{f}}_{\mathrm{NH3}}, \lambda^{\mathrm{f}}_{\mathrm{CO}}$) . Previous works

169   (Peng et al., 2015, 2017) showed that reasonable results can be obtained when the

170   ensemble spread of the emission scaling factors ranged from 0.1 to 1. In order to keep

171   the ensemble spread of the scaling factors at this level in most model area, β is chosen

172   as 1.3, 1.4, 1.3, 1.2, 1.2, and 1.4 for the ensemble concentration ratios of P_{25}, P_{10}, SO_2,

173   NO, NH_3 and CO, respectively in Equation (3).

174   Then, the sources $E_{i,t}^f = (E_{PM2.5}^f, E_{PM10}^f, E_{SO2}^f, E_{NO}^f, E_{NH3}^f, E_{CO}^f)$ are calculated

175   using equation (1).

176   From the perspective of PM2.5 emissions, these include the unspeciated primary

177   sources of PM2.5 $E_{PM2.5}$, sulfate E_{SO4}, and nitrate E_{NO3}. We updated $E_{PM2.5}$, E_{SO4}

178   and E_{NO3} (including the nuclei and accumulation modes) following Peng et al. (2017).

179

180   **2.3 DA algorithm**

181   The assimilation algorithm employed was the EnSRF proposed by Whitaker and Hamill

182   (2002). The EnKF proposed by Evensen (1994) needs perturbations of observations in

183   practice. Compared to the original EnKF, the EnSRF obviates the need to perturb the

184   observations and avoids additional sampling errors introduced by perturbing

185   observations.

186   We used the same EnSRF as in Schwartz et al. (2012, 2014). The ensemble

187   member was chosen as 50. The localization radius was chosen as 607.5 km, so EnSRF

188   analysis increments were forced to zero at 607.5 km away from an observation (Gaspari

189   and Cohn, 1999). The posterior (after assimilation) multiplicative inflation factor was

190   chosen as 1.2 for all the concentration analysis.

191

192   **2.4 State variables**

193   The DA system provides joint analysis of ICs and emissions following Peng et al.

194   (2017). Among them, 16 WRF-Chem/GOCART aerosol variables are included as the

195   state variables. Besides, chemical species, such as SO_2, NO_2 and O_3 are also included

196   because they are the most important gas-phase precursors or oxidants of the secondary

197   inorganic aerosols. CO is also assimilated because CO is an important tracer of

198   combustion sources, as well as a precursor of O_3 beyond NO_2 (Parrish et al., 1991). The

199   state   variables   of   the   emission   scaling   factors   are $\lambda =$

200     $(\lambda_{PM2.5}, \lambda_{PM10}, \lambda_{SO2}, \lambda_{NO}, \lambda_{NH3}, \lambda_{CO})$.

201   Similar to weak-coupling DA, the DA system simultaneously updates both the ICs

202   and the emissions, but with no cross-variable update, in order to avoid the effects of

spurious multivariate correlations in the background error covariance that may develop due to the limited ensemble size and errors in both the model and observations (Miyazaki et al. 2012).

For the PM$_{2.5}$ observations, the observation operator is expressed as (Schwartz et al., 2012)

$$y_{\mathrm{pm25}}^{\mathrm{f}} = \boldsymbol{\rho}_{\mathrm{d}}[\mathbf{P_{25}} + 1.375\mathbf{S} + 1.8(\mathbf{OC_1} + \mathbf{OC_2}) + \mathbf{BC_1} + \mathbf{BC_2}$$
$$+\mathbf{D_1} + 0.286\mathbf{D_2} + \mathbf{S_1} + 0.942\mathbf{S_2}], \qquad (6)$$

where $\boldsymbol{\rho}_{\mathrm{d}}$ is the dry air density; P$_{25}$ is the fine unspectiated aerosol contributions; S represents sulfate; $\mathbf{OC_1}$ and $\mathbf{OC_2}$ are hydrophobic and hydrophilic organic carbon respectively; BC$_1$ and BC$_2$ are hydrophobic and hydrophilic black carbon respectively; $\mathbf{D_1}$ and $\mathbf{D_2}$ are dusts with effective radii of 0.5 and 1.4 μm espectively; S$_1$ and S$_2$ are sea salts with effective radii of 0.3 and 1.0 μm espectively. In fact, PM$_{2.5}$ observations were only used to analyze P$_{25}$, S, OC$_1$, OC$_2$ BC$_1$, BC$_2$, D$_1$, D$_2$, S$_1$, S$_2$ and $\boldsymbol{\lambda}_{\mathrm{PM2.5}}$. Since we had no NH$_3$ observations, PM$_{2.5}$ observations were also used to analyze $\boldsymbol{\lambda}_{\mathrm{NH3}}$ (see Table 2). For other control variables, PM$_{2.5}$ observations were not allowed to alter them.

For the PM$_{10}$ observations, the PM$_{10}$ observation operator is expressed as (Jiang et al., 2013)

$$y_{\mathrm{pm10}}^{\mathrm{f}} = \boldsymbol{\rho}_{\mathrm{d}}[\mathbf{P_{10}} + \mathbf{P_{25}} + 1.375\mathbf{S} + 1.8(\mathbf{OC_1} + \mathbf{OC_2}) + \mathbf{BC_1} + \mathbf{BC_2}$$
$$+\mathbf{D_1} + 0.286\mathbf{D_2} + \mathbf{D_3} + 0.87\mathbf{D_4} + \mathbf{S_1} + 0.942\mathbf{S_2} + \mathbf{S_3}]. \ (7)$$

Thus,

$$y_{\mathrm{pm10-2.5}}^{\mathrm{f}} = \boldsymbol{\rho}_{\mathrm{d}}[\mathbf{P_{10}} + \mathbf{D_3} + 0.87\mathbf{D_4} + \mathbf{S_3}], \qquad (8)$$

meaning that, in the assimilation experiments, we did not use the PM$_{10}$ observations directly. In equation (13) and (14), P$_{10}$ denotes the coarse-mode unspectiated aerosol contributions; D$_3$ and D$_4$ are dusts with effective radii of 2.4 and 4.5 μm respectively; S$_3$ is sea salt with effective radii of 3.25 μm. We used the PM$_{10-2.5}$ observations (the differences between the PM$_{10}$ observations and the PM$_{2.5}$ observations, $y_{\mathrm{pm10-2.5}}^{\mathrm{o}} = y_{\mathrm{pm10}}^{\mathrm{o}} - y_{\mathrm{pm10}}^{\mathrm{o}}$) to analyze P$_{10}$, D$_3$, D$_4$, S$_3$ and $\boldsymbol{\lambda}_{\mathrm{PM10}}$. In addition, PM$_{10-2.5}$ observations were used to analyze D$_5$ and S$_4$, since they are coarse-mode mineral dust

and sea salt aerosols. $PM_{10-2.5}$ observations were not allowed to impact other control variables.

Moreover, as shown in Table 2, SO_2 observations were used to analyze the SO_2 concentration and λ_{SO2}. NO_2 observations were used to estimate the NO, NO_2 concentration and λ_{NO}. CO observations were used to analyze the CO concentration and λ_{CO}. And finally, O_3 observations were only used to analyze the O_3 concentration.

3. Observations and errors

The surface chemical observations used in this study were obtained from the Ministry of Ecology and Environment of China. Altogether, there were 876 observational sites over the model domain (Figure 1). At most sites, one measurement was selected randomly for the assimilation experiment on a $0.1° \times 0.1°$ grid. Altogether, 355 stations were kept for the model domain, where 133 assimilation stations were located on the NCP and 40 stations were located in the Beijing–Tianjin–Hebei (BTH) region. Other stations were used for verification purposes: 167 independent stations were located on the NCP and 47 in the BTH region.

The observation error covariance matrix $\mathbf{R}$ included measurement errors and representation errors. We assumed that $\mathbf{R}$ is a diagonal matrix (without observation correlation).

Following Elbern et al. (2007), the measurement error ε_0 is defined as

$$\varepsilon_0 = a + b * \Pi_0, \tag{9}$$

where Π_0 represents the measurements for $PM_{2.5}$, $PM_{10-2.5}$, SO_2, NO_2, CO or O_3 (units: $\mu g \cdot m^{-3}$). A value of $a = 1.5$ and $b = 0.0075$ was chosen for $PM_{2.5}$, $PM_{10-2.5}$, SO_2, and NO_2. For CO, $a = 10$ and $b = 0.0075$.

The representativeness error is defined as

$$\varepsilon_r = r\varepsilon_0\sqrt{\Delta x/L}, \tag{10}$$

where $r = 0.5$, $\Delta x = 40.5$ km (the model resolution), and $L = 3$ km due to the lack of the information of the station type (Elbern et al., 2007).

Finally, the total error (ε_t) is defined as

$$\varepsilon_{\mathrm{t}} = \sqrt{{\varepsilon_0}^2 + {\varepsilon_r}^2}, \tag{11}$$

In order to ensure data reliability, the observations were subjected to quality control before DA. Data values larger than a certain threshold were classified as unrealistic and were not assimilated. The threshold values were chosen as 700, 800, 300, 300, 400 and 4000 $\mu g \cdot m^{-3}$ for $PM_{2.5}$, $PM_{10\text{-}2.5}$, SO_2, NO_2, O_3 and CO, respectively. In addition, observations leading to innovations exceeding a certain value were also omitted. These threshold values were chosen as 70 $\mu g \cdot m^{-3}$ for $PM_{2.5}$, $PM_{10\text{-}2.5}$, SO_2, NO_2 and O_3. Also, 1500 $\mu g \cdot m^{-3}$ was chosen for CO.

4. Experimental design

The DA experiment followed that of Peng et al. (2017), in which the assimilation of pure surface $PM_{2.5}$ measurements with the EnKF was performed to correct finer aerosol variables and associated emissions. The experiment focused on an extreme haze event that occurred in October 2014 over North China.

The 50-member ensemble spin-up forecasts were first performed from 1 to 4 October 2014 using the perturbed meteorological ICs, lateral boundary conditions (LBCs) and emissions. The perturbed meteorological ICs and LBCs are created by adding Gaussian random noise (Torn et al., 2006) to the temperature, water vapor, velocity, geopotential height and dry surface pressure fields of the products of the National Centers for Environmental Prediction Global Forecast System (GFS) by WRFDA. The perturbed emissions were generated also by adding Gaussian random noise with a standard deviation of 10 percent of the corresponding anthropogenic emissions. The aerosol ICs were zero and the aerosol LBCs were idealized profiles embedded within the WRF-Chem model. And both them are not perturbed (Peng et al., 2017).

Then, the observed PM_{10}, $PM_{2.5}$, SO_2, NO_2, O_3 and CO data starting from 5 to 16 October were assimilated hourly to adjust the ICs and the corresponding emissions. the ICs were the analysis of the previous DA cycle. The meteorological LBCs were perturbed. The anthropogenic emissions, $\mathbf{E}_{\mathrm{PM2.5}}$, $\mathbf{E}_{\mathrm{PM10}}$, $\mathbf{E}_{\mathrm{SO2}}$, $\mathbf{E}_{\mathrm{NO}}$, $\mathbf{E}_{\mathrm{NH3}}$, $\mathbf{E}_{\mathrm{CO}}$,

289 sulfate $\mathbf{E}_{SO4}$ and nitrate $\mathbf{E}_{NO3}$ are calculated by using the forecast emission scaling

290 factors. Other species, such as the organic compounds $\mathbf{E}_{org}$ and elemental compounds

291 $\mathbf{E}_{BC}$, are perturbed by adding Gaussian random noise. Since the emissions are calculated

292 by EQ. (1), their background uncertainties and the spatial correlations are completely

293 dependent on those of the corresponding emission factors. The forecast scaling factors

294 are calculated by EQ. (2) ~ (5). And no other perturbations are added to the scaling

295 factors; no other correlations are assumed for the scaling factors.

296   After that, two sets of 72-h forecasts were performed, each at 00:00 UTC from 6

297 to 15 October 2014, with hourly forecasting outputs for the assimilation experiment.

298 These two sets of forecasting experiments were conducted using the ensemble mean of

299 the concentration analysis as the ICs. One set of the experiments was forced by the

300 optimized emissions (denoted as fcICsEs), and the other was forced by the prescribed

301 anthropogenic emissions (denoted as fcICs). The aim was to use the difference between

302 the fcICsEs and fcICs to indicate the impact of the optimized emissions.

303   Moreover, we also run a control experiment. The ICs were based on the ensemble

304 mean of the spin-up forecasts at 00:00 UTC on 5 October 2014. The emissions were

305 the prescribed emissions.

306

307 **5. Results**

308 5.1 Ensemble performance

309 We begin by assessing the ensemble performance for the DA system. Figure 2 shows

310 the time series of the prior total spreads and the prior root-mean-square errors (RMSEs)

311 for $PM_{2.5}$, PM_{10}, and the four trace gases calculated against all observations in the BTH

312 region. It shows that the magnitudes of the total spreads were close to the RMSEs,

313 indicating that the DA system was well calibrated (Houtekamer et al., 2005).

314   Figure 3 shows the area-averaged time series extracted from the ensemble spread

315 of the six emission scaling factors ($\lambda^f_{PM2.5}$, λ^f_{PM10}, λ^f_{SO2}, λ^f_{NO}, λ^f_{NH3} and λ^f_{CO}) in the

316 BTH region. It shows that the ensemble spread of all the scaling factors were very stable

317 throughout the ~10-day experiment period, which indicates that $\mathbf{M}_{SF}$ can generate

318 stable artificial data to generate the ensemble emissions. The value of the emission

319 scaling factors ranged from 0.2 to 0.6, indicating that the uncertainty of the assimilated

320 emissions was about 20%–60%.

321

322 5.2 Forecast improvements

323 In order to evaluate the overall performance of the DA system, time series of the hourly

324 pollutant concentrations from the control run, the analysis, and the first-day forecast of

325 the two forecasting experiments were compared with the independent observations in

326 the BTH region (Figure 4). Besides, model evaluation statistics (Table 3) were

327 calculated against independent observations from 6 to 16 October 2014. In addition,

328 biases and RMSEs were presented as a function of forecast range for the control,

329 analysis, and forecast experiments (Figures 5–7).

330   The control run did not perform very well, although it was able to capture the

331 synoptic variability and reproduce the overall pollutant levels when there was a severe

332 haze event. The statistics show that there were larger systematic biases and RMSEs and

333 a smaller correlation coefficient (CORR) for the control (see Table 3). The biases were

334 -34.1, -77.7, -565.7 and -31 $\mu g \cdot m^{-3}$ for $PM_{2.5}$, PM_{10}, CO, and O_3, respectively, from

335 6 to 16 October—about 29.7%, 44.5%, 42.9% and 53.9% lower than the corresponding

336 observed concentrations. During the severe haze episode from 8 to 10 October in

337 particular, when observed $PM_{2.5}$ were larger than 200 $\mu g \cdot m^{-3}$, the biases reached -90.5,

338 -143.1, -911.8 and $-39.1 \mu g \cdot m^{-3}$, respectively—about 44.4%, 51.9%, 49.2% and 55.7%

339 lower than the corresponding observed concentrations, suggesting a significant

340 systematic underestimation of the WRF-Chem simulation. Additionally, a significant

341 overestimation of 48.1 $\mu g \cdot m^{-3}$ was obtained for SO_2—about 145.8% higher than the

342 observed concentrations. As for the NO_2 simulation, WRF-Chem was able to

343 realistically describe the diurnal and synoptic evolution of NO_2 concentrations. The

344 model bias was 22.4 $\mu g \cdot m^{-3}$, which was about 39.7% higher than the observed NO_2.

345 These results were similar to the simulations of Chen et al. (2016). Most of the WRF-

346 Chem settings used here were the same as those used in Chen et al. (2016), except that

347 they used CBMZ (Carbon Bond Mechanism, version Z) and MOSAIC (Model for

348 Simulating Aerosol Interactions and Chemistry) as the gas-phase and aerosol chemical

349   mechanisms.

350   After the assimilation of surface observations, the time series of the hourly

351   pollutant concentrations from the analysis showed much better agreement with

352   observations than those from the control. The magnitudes of the bias and the RMSEs

353   decreased and the CORRs increased for all six species. The biases were 5.1, −5.6, 8.1,

354   −8.3, −160.4 and 2.1 $\mu g \cdot m^{-3}$ for $PM_{2.5}$, PM_{10}, SO_2, NO_2, CO and O_3, respectively—

355   about 4.4%, −3.2%, 24.5%, −14.7%, −12.17% and 3.7% of the corresponding observed

356   concentrations, indicating that the analysis fields were very close to the observations.

357   The RMSEs were 51.5, 63.4, 27.9, 31.7, 618.9 and 31.1 $\mu g \cdot m^{-3}$, respectively—about

358   44.1%, 52.9%, 58.1%, 20.2%, 35.7% and 38.78% lower than the RMSEs of the control

359   run. The CORRs reached 0.891, 0.890, 0.540, 0.557, 0.705 and 0.753, respectively.

360   These statistics indicate that the DA system was able to adjust the chemical ICs

361   efficiently.

362   The $PM_{2.5}$, PM_{10} and CO concentrations from both sets of forecasting experiments

363   benefitted substantially from the DA procedure, as expected. Smaller biases and

364   RMSEs were obtained for almost the entire 72-h forecast range (see Figures 5–7), as

365   compared with the control run. For the first-day forecast in particular, the model

366   performed almost perfectly. It faultlessly captured the diurnal and synoptic variability

367   of the pollutant (see figure 4), in a manner that was very close to that of the analysis.

368   The overall biases were 6.5, −11.9 and 100.4 $\mu g \cdot m^{-3}$ for $PM_{2.5}$, PM_{10} and CO,

369   respectively; and the RMSEs were 77.8, 98.7 and 805.1 $\mu g \cdot m^{-3}$, respectively, in

370   fcICsEs24 (see Table 3). In fcICs24, the biases were 8.3, −10.3 and 130.2 $\mu g \cdot m^{-3}$,

371   respectively; and the RMSEs were 75.1, 95.9 and 838.2 $\mu g \cdot m^{-3}$, respectively (see Table

372   3). However, with longer-range forecasts, the impact of DA quickly decayed. The

373   relative reductions in RMSE mostly ranged from 30% to 5% for the second- and third-

374   day forecast. From the perspective of the impact of the assimilated emissions, fcICs

375   performed similarly to fcICsEs for $PM_{2.5}$, PM_{10} and CO, indicating that ICs play key

376   roles in aerosol and CO forecasts during severe haze episodes, while the impact of

377   assimilated emissions seems negligible.

378   For the SO_2 verification forecast, however, fcICsEs performed much better than

379 both fcICs and the control run. Smaller biases and RMSEs were obtained for almost the

380 entire 72-h forecast range. At nighttime in particular (from 18 to 23 h, 42 to 47 h, and

381 66 to 73 h), when there was significant systematic overestimation in the control run,

382 both the biases and the RMSEs in fcICsEs were about 30% lower than those of the

383 control run. During the daytime (from 0 to 9 h, 24 to 33 h, and 48 to 57 h), fcICsEs still

384 performed slightly better, although the control run did a near perfect job. As for fcICs,

385 smaller biases and RMSEs were obtained for only the first 3 h. Then, the performance

386 was the same as the control run, indicating that the impact of the ICs had disappeared.

387 These results demonstrate the superiority of the assimilated emissions, and that the joint

388 adjustment of SO_2 ICs and emissions is an efficient way to improve the SO_2 forecast.

389 The NO_2 DA results for the independent sites showed really poor performance

390 (see Figures 5–7). Smaller biases were gained in the daytime of the experiment trials.

391 At nighttime, however, when the simulated NO_2 deviated considerably from the

392 observations in the control run, the biases of both sets of the validation forecasts became

393 even larger. Besides, almost all the RMSEs of both sets of the validation forecasts were

394 always larger than those of the control run.

395 The O_3 DA results were dependent on the NO_2 DA results in the daytime, due to

396 chemical transformation. Both the biases and the RMSEs were larger, as compared with

397 those of the control run (see Figures 5–7). However, at nighttime, when there was

398 significant systematic underestimation in the control run, the biases in fcICsEs had very

399 similar values to those of the analysis. Also, the biases in fcICs ranged between the

400 analysis and the control run; and the RMSEs of both sets of forecasting experiments

401 were about 10% smaller than those of the control run. All these results indicate that the

402 DA system performed well at night.

403

404 5.3 Emission optimization results

405 Besides improved pollutant forecasts, improved estimates of emissions were expected

406 from the joint DA procedure. The MEIC-2010 was constructed on the basis of annual

407 statistical books in which the data were often 2–3 years older than the actual year (Chen

408 et al., 2016). However, consistent efforts aimed at reducing and managing

409   anthropogenic emissions have been made over the past decade to mitigate air pollution.

410   Thus, there was a large difference between the emission year and our simulation year.

411   Besides, the spatial allocations of these emissions over small spatial scales, and the

412   monthly allocations, will also lead to some uncertainties. Lastly, the emissions

413   inventory cannot fully capture the day-to-day variability or the actual daily variations,

414   though its differentiation in terms of working days and weekend days, plus the daily

415   variations, can be taken into account in practical applications. However, in this

416   assimilation procedure, the differentiation in terms of working days and weekend days,

417   plus the daily variations, was ignored. Therefore, the prescribed anthropogenic

418   emissions were subject to large uncertainties.

419   Figures 8 and 9 display the spatial distribution of the prescribed emission rates and

420   the differences between the analysis and the prescribed emission rates of $PM_{2.5}$, PM_{10},

421   NH_3, SO_2, NO and CO averaged over all hours from 6 to 16 October 2014 in the NCP

422   region. The assimilated emission rates of $PM_{2.5}$, SO_2, NO and CO were lower than the

423   prescribed emissions on the whole. In the BTH region especially, the differences

424   reached -0.02 $\mu g \cdot m^{-2} \cdot s^{-1}$, -2.9, -8.8 and -24.65 $mol \cdot km^{-2} \cdot hr^{-1}$, which was a reduction

425   of about 10%–20% of the prescribed emissions. For PM_{10} emissions, the assimilated

426   values were very close to the prescribed ones, indicating that the prescribed PM_{10}

427   emissions had small uncertainties for the NCP region. For NH_3 emissions, the

428   assimilated values were a little larger than the prescribed emissions in large industrial

429   cities like Beijing, Tianjin, Baoding, Xingtai, Handan, and Taiyuan. However, they

430   were smaller than the prescribed emissions in agricultural regions, especially in

431   Shandong Province and Henan Province. However, in the BTH region, the assimilated

432   NH_3 emissions were very close to the prescribed emissions on the whole.

433   Figure 10 shows the time series of the emission scaling factors and the emissions.

434   As concluded in Peng et al. (2017), the forecast emission scaling factors changed with

435   the analyzed emission scaling factors due to the use of the time smoothing operator.

436   Besides, although the prescribed emissions were constant when designing the

437   assimilation experiment, the analyzed emission scaling factors showed obvious

438   variation with time, as did the analyzed emissions. For the assimilated SO_2 and NO

emissions in particular, the diurnal variations were perfect. In addition, the difference between the assimilated emissions and the prescribed emissions were consistent with those in Figures 8 and 9. The assimilated emissions of $PM_{2.5}$, SO_2, NO and CO were apparently lower than the corresponding prescribed emissions. Whereas, the values of the assimilated emissions of PM_{10} and NH_3 were very close to their corresponding prescribed emissions.

In order to investigate the impact of optimized emissions on chemical simulations, a simulation (fcEs) using the optimized emissions were performed from 5 to 16 October 2014. Same as the control run, the ICs were the ensemble mean of the spin-up forecasts at 00:00 UTC on 5 October 2014. Thus the difference between the fcEs and the control run is the anthropogenic emissions. The results showed that the fcEs performed very similar to the control run in the whole in the BTH region. For $PM_{2.5}$, PM_{10} and CO, the values of the fcEs were a little smaller than those of the control run, which were consistent with the difference of the anthropogenic emissions. For SO_2 and NO_2, fcEs performed much better than the control run in most time though significant systematic overestimation still existed during the nighttime. For O_3, miner improvements were also gained due to the better simulation in fcEs for NO_2.

5.4 Discussion

From the results presented above, it is clear that improvements were achieved for almost all the 72-h verification forecasts using the optimized ICs and emissions for $PM_{2.5}$, PM_{10}, SO_2 and CO concentrations in the BTH region. However, the 72-h NO_2 verification forecasts performed much worse than the control run, due to the assimilation. Plus, the 72-h O_3 verification forecasts performed worse than the control run during the daytime, due to the worse performance of the NO_2 forecasts, although they did perform better at night. However, relatively favorable NO_2 and O_3 forecast results were gained for the Yangtze River delta and Pearl River delta (PRD) regions (see Figure 11). In the PRD region, during the daytime, the three NO_2 forecasts (i.e., the control run, the fcICsEs, and the fcICs) performed similarly, and had relatively small biases and RMSEs. At nighttime, when there was significant systematic

469   overestimation in the control run, the biases and the RMSEs in fcICsEs were much

470   smaller than those in the control run. For the O_3 72-h verification forecasts, fcICsEs

471   performed much better than the control run, except for the first 8 h. Also, fcICs

472   improved the O_3 forecasts to some extent from the 9- to 72-h forecast range. These

473   results indicate that DA is still an effective way to improve NO_2 and O_3 forecasts.

474   Regarding the failure to improve the NO_2 and O_3 forecasts in the BTH region,

475   there are three likely factors. And certainly, NO_2 and O_3 forecasts in other areas are also

476   facing similar challenges.

477   Firstly, there are still some limitations for the EnKF method. EnKF assimilation is

478   influenced greatly by model errors and observation errors. There are many sources of

479   uncertainties in air-quality forecast that were not directly considered in this study (such

480   as chemical schemes and parameterizations, meteorology, and emissions). And it is

481   very difficult to accurately evaluate the uncertainties of models, though the covariance

482   inflation technique was simply applied for all state variables to roughly compensate for

483   model errors. Therefore, we can only obtain suboptimal results through EnKF

484   assimilation. Furthermore, for short-lived chemical reactive species, such as NO_2 and

485   O_3, they undergo highly complex nonlinear photochemical reactions, even

486   on timescales of hours, such that the forecast accuracy is largely dependent on the

487   chemical process as well as the physical transportation process, the ICs, and the

488   emissions. However, those complex photochemical reaction processes are not precisely

489   described in current chemical mechanisms, e.g., heterogeneous reactions (Yang et al.,

490   2015), the photolysis of nitrous acid and $ClNO_2$ during daytime (Zhang et al., 2017),

491   and so on. Therefore, on the one hand, there are still large uncertainties for NO_2 and O_3

492   forecasts; whilst on the other hand, it is very difficult for NO_2 and O_3 DA to accurately

493   estimate the model errors with a limited ensemble size. Thus, NO_2 and O_3 assimilations

494   do not perform well (Elbern et al., 2007; Tang et al., 2016). However, for SO_2 and CO,

495   which are representative of long-lived chemical reactive species, the chemical reaction

496   process does not work on timescales of hours, meaning that to some extent hourly

497   chemical DA has the potential to improve their forecasts. For CO in particular, due to

498   its inertness, we might be able to obtain high-quality ICs and emissions through DA.

The primary sources of aerosol are the dominant part of the atmospheric aerosol concentration. So, 72-h aerosol forecasts may perform similarly to CO, albeit there are large uncertainties in the chemical model.

Secondly, as stated in the above paragraph, the analysis ICs and emissions are only a mathematical optimum under the existing conditions. In addition, only part of the chemical ICs and emissions are involved in the DA experiment; and VOC ICs and emissions, which may greatly influence the NO_2 and O_3 forecasts, were not included here because of the absence of VOC measurements. Although we carried out two DA sensitivity experiments to adjust the VOC ICs and emissions through the use of NO_2 or O_3 measurements, we were still unable to gain improved NO_2 and O_3 forecasts in the BTH region in both DA experiments. VOC measurements are needed to reduce uncertainties of VOC ICs and emissions. In addition, almost all available data were observed in cities, and no observation stations located in rural. Thus, the atmospheric environmental monitoring system was still spatially heterogeneous.

Another important point is that there are still limitations to the current chemical mechanisms used in our model, such as the treatment of model error. NO is the primary species of NO_x emissions in city areas, and reacts directly with O_3 to form NO_2 ($NO+O_3 \rightarrow NO_2+O_2$). Thus, O_3 concentrations may inversely correlate with NO_2 concentrations at night. Consequently, air quality models may systematically underestimate O_3 concentrations. Currently, DA can only revise the ICs and the emissions in this work. It cannot change the model performance, especially when there are certain uncertainties for the meteorological simulation.

6. Summary

In this study, we developed an EnKF system to simultaneously assimilate surface measurements of PM_{10}, $PM_{2.5}$, SO_2, NO_2, O_3 and CO via the joint adjustment of ICs and source emissions. This system was applied to assimilate hourly pollution data while modeling an extreme haze event that occurred in early October 2014 over North China. In order to evaluate the impact of DA, two sets of 72-h verification forecasts were performed. One was conducted with the optimized ICs and emissions, and the other

529 with only optimized ICs and the prescribed emissions. A control experiment without

530 DA was also performed for comparison.

531   The results showed that both verification forecasts performed much better than the

532 control simulations for $PM_{2.5}$, PM_{10} and CO. Obvious improvements were achieved for

533 almost the entire 72-h forecast range. For the first-day forecast especially, near perfect

534 forecasts results were achieved. However, with longer-range forecasts, the impact of

535 DA quickly decayed. In addition, the forecasts with only optimized ICs and the

536 prescribed emissions performed similarly to that with the optimized ICs and emissions,

537 indicating that ICs play key roles in $PM_{2.5}$, PM_{10} and CO forecasts during severe haze

538 episodes.

539   Also, large improvements were achieved for SO_2 forecasts with both the optimized

540 ICs and emissions for the whole 72-h forecast range. However, similar improvements

541 were achieved for SO_2 forecasts with the optimized ICs only for just the first 3 h, and

542 then the impact of the ICs decayed quickly to zero. This demonstrates that the joint

543 adjustment of SO_2 ICs and emissions is an efficient way to improve SO_2 forecasts.

544   Even though we failed to improve the NO_2 and O_3 forecasts in the BTH region,

545 relatively favorable NO_2 and O_3 forecast results were gained in other areas. Also, the

546 forecasts with both the optimized ICs and emissions performed much better than the

547 forecasts with only optimized ICs and the prescribed emissions. These results indicate

548 that there is still potential to improve NO_2 and O_3 forecasts via the joint adjustment of

549 SO_2 ICs and emissions.

550   However, only a case was investigated in this work. Thus it is uncertain if the

551 conclusions about different performance of forecasts for various species would hold in

552 a general. Therefore, more case studies are needed to obtain general conclusions in

553 future works.

554

555 **Data availability.** To reproduce the data presented in the draft, the WRF-Chem model

556 version 3.6.1 can be downloaded at

557 http://www2.mmm.ucar.edu/wrf/users/download/get_source.html; the meteorological

558 background is provided by GFS data (0.5°) which can be downloaded from

559 https://www.ncdc.noaa.gov/data-access/model-data/model-datasets/global-forcast-

560 system-gfs; the observations are available from

561 http://113.108.142.147:20035/emcpublish/.

562 **Competing interests.** The authors declare that they have no conflict of interest.

563 **Acknowledgements.** The authors are grateful to the two anonymous reviewers for their

564 precious suggestions. This work was supported by the National Key Technologies

565 Research and Development program of China (2016YFC0202102), and the National

566 Natural Science Foundation of China (41875014, 41575141 and 41675052). The

567 National Center for Atmospheric Research is sponsored by US National Science

568 Foundation. The numerical calculations in this paper were carried out on the IBM Blade

569 cluster system in the High Performance Computing Center (HPCC) of Nanjing

570 University.

571 **Author contributions.** Zhen Peng and Zhiquan Liu planned the research and

572 developed the algorithm. Zhen Peng, Jianning Sun and Aijun Ding designed the

573 experiments. Zhen Peng, Lili Lei and Junmei Ban developed the model code. Zhen

574 Peng and Kekuan Chu performed the simulations and analysis. Dan Chen provided the

575 anthropogenic emissions for the model. Xingxia Kou performed the quality control

576 procedure for the observations. Zhen Peng prepared the manuscript with contributions

577 from all co-authors.

578

579 **References**

580 Barbu, A. L., Segers, A. J., Schaap, M., Heemink, A.W., and Builtjes, P. J. H.: A multi-component data assimilation
581 experiment directed to sulphur dioxide and sulphate over Europe, Atmos. Environ., 43, 1622–1631, 2009.

582 Carmichael, G. R., Daescu, D. N., Sandu, A., and Chai, T.: Computational aspects of chemical data assimilation into
583 atmospheric models, in Science Computational ICCS 2003. Lecture Notes in Computer Science, IV, 269–278,
584 Springer, Berlin, 2003.

585 Carmichael, G. R., Sandu, A., Chai, T., Daescu, D. N., Constantinescu, E. M., and Tang, Y.: Predicting air quality:
586 improvements through advanced methods to integrate models and measurements, J. Comput. Phys., 227, 3540–
587 3571, 2008a.

588 Carmichael, G. R., Sakuraib, T., Streetsc, D., Hozumib, Y., Uedab, H., Parkd, S. U., Funge, C., Hanb, Z., Kajinof,
589 M., Engardtg, M., Bennetg, C., Hayamih, H., Sarteleti, K., Hollowayj, T., Wangk, Z., Kannaril, A., Fum, J.,
590 Matsudan, K., Thongboonchooa, N., and Amanno, M.: MICS-ASIA II: the model intercomaprison study for
591 Asia phase II methodology and overview of findings, Atmos. Environ., 42, 3468–3490, 2008b.

592 Chai, T., Carmichael, G. R., Tang, Y., Sandu, A., Hardesty, M., Pilewskie, P., Whitlow, S., Browell, E. V., Avery,

593   M. A., Nedelec, P., Merrill, J. T., Thompson, A. M., and Williams, E.: Four dimensional data assimilation
594   experiments with International Consortium for Atmospheric Research on Transport and Transformation ozone
595   measurements, J. Geophys. Res., 112, D12S15, doi:10.1029/2006JD007763, 2007.

596 Chen, D., Liu, Z., Fast, J., and Ban, J.: Simulations of sulfate – nitrate – ammonium (SNA) aerosols during the
597   extreme haze events over northern China in October 2014, Atmos. Chem.Phys., 16, 10707 – 10724,
598   doi:10.5194/acp-16-10707-2016, 2016.

599 Chen, F. and Dudhia, J.: Coupling an advanced land surfacehydrology model with the Penn State-NCAR MM5
600   modeling system. Part I: Model implementation and sensitivity, Mon. Weather Rev., 129, 569 – 585,
601   doi:10.1175/1520-0493(2001)129<0569:Caalsh>2.0.Co;2, 2001.

602 Chin, M., Rood, R. B., Lin, S. J., Muller, J. F., and Thompson,A. M.: Atmospheric sulfur cycle simulated in the
603   global model GOCART: Model description and global properties, J. Geophys. Res.-Atmos., 105, 24671 –
604   24687, 2000.

605 Chin, M., Ginoux, P., Kinne, S., Torres, O., Holben, B. N., Duncan, B. N., Martin, R. V., Logan, J. A., Higurashi,
606   A., and Nakajima, J.: Tropospheric aerosol optical thickness from the GOCART model and comparisons with
607   satellite and Sun photometer measurements, J. Atmos. Sci., 59, 461 – 483, 2002.

608 Chou, M.-D. and Suarez, M. J.: An efficient thermal infrared radiation parameterization for use in general circulation
609   models, NASA Tech. Memo., TM 104606, vol. 3, 25 pp., NASA Goddard Space Flight Cent., Greenbelt, MD,
610   USA, 1994.

611 Dai, T., Schutgens, N. A. J., Goto, D., Shi, G. Y., and Nakajima, T.: Improvement of aerosol optical properties
612   modeling over Eastern Asia with MODIS AOD assimilation in a global non-hydrostatic icosahedral aerosol
613   transport model, Environ. Pollut., 195, 319–329, 2014.

614 Ding, A. J., Huang, X., Nie, W., Sun, J., Kerminen, V. M., Petaja, T., Su, H. L., Cheng, Y. F., Yang, X. Q., and
615   Wang, M.: Enhanced haze pollution by black carbon in megacities in China, Geophys. Res. Lett., 2873-2879,
616   doi:10.1002/2016GL067745, 2016.

617 Ding, J., van der A, R. J., Mijling, B., Levelt, P. F., and Hao, N.: NO_x emission estimates during the 2014 Youth
618   Olympic Games in Nanjing, Atmos. Chem. Phys., 15, 9399–9412, doi:10.5194/acp-15-9399-2015, 2015.

619 Elbern, H., Schmidt, H., and Ebel, A.: Variational data assimilation for tropospheric chemistry modelling, J. Geophys.
620   Res., 102, 15967–15985, 1997.

621 Elbern, H. and Schmidt, H.: A 4D-Var chemistry data assimilation scheme for Eulerian chemistry transport
622   modelling, J. Geophys. Res., 104, 18583–18598, 1999.

623 Elbern, H., Schmidt, H., Talagrand, O., and Ebel, A.: 4D-variational data assimilation with an adjoint air quality
624   model for emission analysis, Environ, Model. Softw., 15, 539–548, 2000.

625 Elbern, H. and Schmidt, H.: Ozone episode analysis by four dimensional variational chemistry data assimilation, J.
626   Geophys. Res., 106, 3569–3590, 2001.

627 Elbern, H., Strunk, A., Schmidt, H., and Talagrand, O.: Emission rate and chemical state estimation by 4-dimensional
628   variational inversion, Atmos. Chem. Phys., 7, 3749–3769, doi:10.5194/acp-7-3749-2007, 2007.

629 Evensen, G.: Sequential data assimilation with a nonlinear quasigeostrophic model using Monte Carlo methods to
630   forecast error statistcs, J. Geophys. Res., 99, 10143 – 10162, 1994.

631 Gaspari, G. and Cohn S. E.: Construction of correlation functions in two and three dimensions, Quart. J. R. Meteorol.
632   Soc. 125 (1999), 723–757.

633 Ginoux, P., Chin, M., Tegen, I., Prospero, J. M., Holben, B., Dubovik, O., and Lin, S.-J.: Sources and distributions
634   of dust aerosols simulated with the GOCART model, J. Geophys. Res., 106, 20255 – 20273,
635   doi:10.1029/2000JD000053, 2001.

636 Grell, G., Peckham, S. E., Schmitz, R., McKeen, S. A., Frost, G., Skamarock, W. C., and Eder, B.: Fully coupled

637   "online" chemistry within the WRF model, Atmos. Environ., 39, 6957–6975,
638   doi:10.1016/j.atmosenv.2005.04.027, 2005.

639   Guenther, A., Hewitt, C. N., Erickson, D., Fall, R., Geron, C., Graedel, T., Harley, P., Klinger, L., Lerdau, M.,
640   McKay, W., Pierce, T., Scholes, B., Steinbrecher, R., Tallamraju, R., Taylor, J., and Zimmerman, P.: A global
641   model of natural volatile organic compound emissions, J. Geophys. Res., 100, 8873–8892,
642   doi:10.1029/94JD02950, 1995.

643   Guerrette, J. J. and Henze, D. K.: Development and application of the WRFPLUS-Chem online chemistry adjoint
644   and WRFDA-Chem assimilation system, Geosci. Model Dev., 8, 1857–1876, doi:10.5194/gmd-8-1857-2015,
645   2015.

646   Hakami, A., Henze, D. K., Seinfeld, J. H., Chai, T., Tang, Y., Carmichael, G. R., and Sandu, A.: Adjoint inverse
647   modeling of black carbon during the Asian Pacific Regional Aerosol Characterization Experiment, J. Geophys.
648   Res.-Atmos., 110, D14301, doi:10.1029/2004JD005671, 2005.

649   Heemink, A.W. and Segers, A. J.: Modeling and prediction of environmental data in space and time using Kalman
650   filtering, Stoch. Environ. Res. Risk A., 16, 225–240, 2002.

651   Henze, D. K., Hakami, A., and Seinfeld, J. H.: Development of the adjoint of GEOS-Chem, Atmos. Chem. Phys., 7,
652   2413–2433, doi:10.5194/acp-7-2413-2007, 2007.

653   Henze, D. K., Seinfeld, J. H., and Shindell, D. T.: Inverse modeling and mapping US air quality influences of
654   inorganic $PM_{2.5}$ precursor emissions using the adjoint of GEOS-Chem, Atmos. Chem. Phys., 9, 5877–5903,
655   doi:10.5194/acp-9-5877-2009, 2009.

656   Hong, S. Y., Noh, Y., and Dudhia, J.: A new vertical diffusion package with an explicit treatment of entrainment
657   processes, Mon. Weather Rev., 134, 2318–2341, doi:10.1175/Mwr3199.1, 2006.

658   Houtekamer, P. L., Mitchell, H. L., Pellerin, G., Buehner, M., Charron, M., Spacek, L., and Hansen, B.: Atmospheric
659   data assimilation with an ensemble Kalman filter: Results with real observations, Mon. Weather Rev., 133,
660   604–620, 2005.

661   Huang, X., Song, Y., Zhao, C., Li, M., Zhu, T., Zhang Q., and Zhang, X.Y.: Pathways of sulfate enhancement by
662   natural and anthropogenic mineral aerosols in China, J. Geophys. Res.–Atmos., 119, 24, 14165-14179, 2014.

663   Jiang, Z., Liu, Z., Wang, T., Schwartz, C. S., Lin, H.-C., and Jiang, F.: Probing into the impact of 3DVAR
664   assimilation of surface PM_{10} observations over China using process analysis, J. Geophys. Res.-Atmos., 118,
665   6738–6749, doi:10.1002/jgrd.50495,2013.

666   Li, Z., Zang, Z., Li, Q. B., Chao, Y., Chen, D., Ye, Z., Liu, Y., and Liou, K. N.: A three-dimensional variational data
667   assimilation system for multiple aerosol species with WRF/Chem and an application to $PM_{2.5}$ prediction, Atmos.
668   Chem. Phys., 13, 4265–4278, doi:10.5194/acp-13-4265-2013, 2013.

669   Li, M., Zhang, Q., Streets, D. G., He, K. B., Cheng, Y. F., Emmons, L. K., Huo, H., Kang, S. C., Lu, Z., Shao, M.,
670   Su, H., Yu, X., and Zhang, Y.: Mapping Asian anthropogenic emissions of nonmethane volatile organic
671   compounds to multiple chemical mechanisms, Atmos. Chem. Phys., 14, 5617–5638, doi:10.5194/acp-14-
672   5617-2014, 2014

673   Liu, Z., Liu, Q., Lin, H. C., Schwartz, C. S., Lee, Y. H., and Wang, T.: Three-dimensional variational assimilation
674   of MODIS aerosol optical depth: implementation and application to a dust storm over East Asia, J. Geophys.
675   Res., 116, D23206, doi:10.1029/2011JD016159, 2011.

676   McLinden, C.A., Fioletov, V., Shephard, M.W., Krotkov, N., Li, C., Martin, R.V., Moran, M.D., and J. Joiner,: Space-
677   based detection of missing sulfur dioxide sources of global air pollution, Nat. Geosci., 9, 496–500,
678   doi:10.1038/ngeo2724, 2016.

679   Mijling, B., van der A, R. J., Boersma, K. F., Van Roozendael, M., De Smedt, I., and Kelder, H. M.: Reduction of
680   NO_2 detected from space during the 2008 Beijing Olympic Games, Geophys. Res. Lett., 36, L13801,

doi:10.1029/2009GL038943, 2009.

Mijling, B. and van der A, R. J.: Using daily satellite observations to estimate emissions of short-lived air pollutants on a mesoscopic scale, J. Geophys. Res., 117, D17302, doi:10.1029/2012JD017817, 2012.

Mijling, B., van der A, R. J., and Zhang, Q.: Regional nitrogen oxides emission trends in East Asia observed from space, Atmos. Chem. Phys., 13, 12003–12012, doi:10.5194/acp-13-12003-2013, 2013.

Miyazaki, K., Eskes, H. J., Sudo, K., Takigawa, M., van Weele, M., and Boersma, K. F.: Simultaneous assimilation of satellite NO_2, O_3, CO, and HNO_3 data for the analysis of tropospheric chemical composition and emissions, Atmos. Chem. Phys., 12, 9545– 9579, doi:10.5194/acp-12-9545-2012, 2012.

Miyazaki, K. and Eskes, H.: Constraints on surface NO_x emissions by assimilating satellite observations of multiple species, Geophys. Res. Lett., 40, 4745–4750, doi:10.1002/grl.50894, 2013.

Miyazaki, K., Eskes, H. J., Sudo, K., and Zhang, C.: Global lightning NO_x production estimated by an assimilation of multiple satellite data sets, Atmos. Chem. Phys., 14, 3277–3305, doi:10.5194/acp-14-3277-2014, 2014.

Mlawer, E. J., Taubman, S. J., Brown, P. D., Iacono, M. J., and Clough, S. A.: Radiative transfer for inhomogeneous atmospheres: RRTM, a validated correlated-k model for the longwave, J. Geophys. Res.-Atmos., 102, 16663–16682, doi:10.1029/97jd00237, 1997.

Nie, W., Ding, A., Wang, T., Kerminen, V.-M., George, C., Xue, L., Wang, W., Zhang, Q., Petäjä, T., Qi, X., Gao, X., Wang, X., Yang, X., Fu, C., and Kulmala, M.: Polluted dust promotes new particle formation and growth, Sci. Rept., 4, 6634, 2014.

Pagowski, M., Grell, G. A., McKeen, S. A., Peckham, S. E., and Devenyi, D.: Three-dimensional variational data assimilation of ozone and fine particulate matter observations: some results using the Weather Research and Forecasting – Chemistry model and Grid-point Statistical Interpolation, Q. J. Roy. Meteor. Soc., 136, 2013–2024, doi:10.1002/qj.700, 2010.

Pagowski, M., and Grell, G. A.: Experiments with the assimilation of fine aerosols using an ensemble Kalman filter, J. Geophys. Res.-Atmos., 117, D21302, doi:10.1029/2012jd018333, 2012.

Pagowski, M., Liu, Z., Grell, G. A., Hu, M., Lin, H.-C., and Schwartz, C. S.: Implementation of aerosol assimilation in Gridpoint Statistical Interpolation (v. 3.2) and WRF-Chem (v.3.4.1), Geosci. Model Dev., 7, 1621-1627, https://doi.org/10.5194/gmd-7-1621-2014, 2014.

Parrish, D. D., M. Trainer, M. P. Buhr, B. A. Watkins, and F. C. Fehsenfeld, Carbon monoxide concentrations and their relation to concentrations of total reactive oxidized nitrogen at two rural U.S. sites, J. Geophys. Res., 96, 9309– 9320, 1991.

Parrish, D. D., and Zhu, T.: Clean Air for Megacities, Science, 326, 674-675, 408 doi:10.1126/science.1176064, 2009.

Peng, Z., Zhang, M., Kou, X., Tian, X., and Ma, X.: A regional carbon data assimilation system and its preliminary evaluation in East Asia, Atmos. Chem. Phys., 15, 1087-1104, doi:10.5194/acp-15-1087-2015, 2015.

Peng, Z., Liu, Z., Chen, D., and Ban, J.: Improving PM2. 5 forecast over China by the joint adjustment of initial conditions and source emissions with an ensemble Kalman filter, Atmos. Chem. Phys., 17, 4837-4855, https://doi.org/10.5194/acp-17-4837-2017, 2017.

Pope, C. A.: Review: Epidemiological basis for particulate air pollution health standards, Aerosol Sci. Tech., 32, 4–14, 2000.

Pope, C. A., Burnett, R. T., Thun, M. J., Calle, E. E., Krewski, D., Ito, K., and Thurston, G. D.: Lung cancer, cardiopulmonary mortality, and long-term exposure to fine particulate air pollution, J. Am. Med. Assoc., 287, 1132–1141, 2002.

Sandu, A., Daescu, D., Carmichael, G. R., and Chai, T.: Adjoint sensitivity analysis of regional air quality models, J. Comput. Phys., 204, 222–252, 2005.

Schutgens, N. A. J., Miyoshi, T., Takemura, T., and Nakajima, T.: Sensitivity tests for an ensemble Kalman filter for aerosol assimilation, Atmos. Chem. Phys., 10, 6583–6600, doi:10.5194/acp-10-6583-2010, 2010a.

Schutgens, N. A. J., Miyoshi, T., Takemura, T., and Nakajima, T.: Applying an ensemble Kalman filter to the assimilation of AERONET observations in a global aerosol transport model, Atmos. Chem. Phys., 10, 2561–2576, doi:10.5194/acp-10-2561-2010, 2010b.

Schutgens, N., Nakata, M., and Nakajima, T.: Estimating Aerosol Emissions by Assimilating Remote Sensing Observations into a Global Transport Model, Remote Sens., 4, 3528–3543, 2012.

Schwartz, C. S., Liu, Z., Lin, H. C., and McKeen, S. A.: Simultaneous three-dimensional variational assimilation of surface fine particulate matter and MODIS aerosol optical depth, J. Geophys. Res., 117, D13202, doi:10.1029/2011JD017383, 2012.

Schwartz, C. S., Liu, Z., Lin, H.-C., and Cetola, J. D.: Assimilating aerosol observations with a "hybrid" variational-ensemble data assimilation system, J. Geophys. Res.-Atmos., 119, 4043–4069, doi:10.1002/2013JD020937, 2013.

Sekiyama, T. T., Tanaka, T. Y., Shimizu, A., and Miyoshi, T.: Data assimilation of CALIPSO aerosol observations, Atmos. Chem. Phys., 10, 39-49, doi:10.5194/acp-10-39-2010, 2010.

Stockwell, W. R., Kirchner, F., Kuhn, M., and Seefeld, S: A new mechanism for regional atmospheric chemistry modeling, J. Geophys. Res., 102(D22), 25,847–25,879, doi:10.1029/97JD00849, 1997.

Sun, Y. L., Wang, Z. F., Du, W., Zhang, Q., Wang, Q. Q., Fu, P. Q., Pan, X. L., Li, J., Jayne, J., and Worsnop, D. R.: Longterm real-time measurements of aerosol particle composition in Beijing, China: seasonal variations, meteorological effects, and source analysis, Atmos. Chem. Phys., 15, 10149–10165, doi:10.5194/acp-15-10149-2015, 2015.

Tang, X., Wang, Z. F., Zhu, J., Gbaguidi, A., Wu, Q. Z., Li, J., and Zhu, T.: Sensitivity of ozone to precursor emissions in urban Beijing with a Monte Carlo scheme, Atmos. Environ., 44, 3833–3842, 2010.

Tang, X., Zhu, J., Wang, Z. F., and Gbaguidi, A.: Improvement of ozone forecast over Beijing based on ensemble Kalman filter with simultaneous adjustment of initial conditions and emissions, Atmos. Chem. Phys., 11, 12901–12916, doi:10.5194/acp-11-12901-2011, 2011.

Tang, X., Zhu, J., Wang, Z. F., Wang, M., Gbaguidi, A., Li, J., Shao, M., Tang, G.Q., and Ji, D.S.: Inversion of CO emissions over Beijing and its surrounding areas with ensemble Kalman filter, Atmos. Environ., 81, 676–686, 2013.

Tang, X., Zhu, J., Wang, Z., Gbaguidi, A., Lin, C., Xin, J., Song, T., and Hu, B.: Limitations of ozone data assimilation with adjustment of NO_x emissions: mixed effects on NO_2 forecasts over Beijing and surrounding areas, Atmos. Chem. Phys., 16, 6395-6405, https://doi.org/10.5194/acp-16-6395-2016, 2016.

van der A, R. J., Peters, D. H. M. U., Eskes, H., Boersma, K. F., Van Roozendael, M., De Smedt, I., and Kelder, H. M.: Detection of the trend and seasonal variation in tropospheric NO_2 over China, J. Geophys. Res., 111, D12317, doi:10.1029/2005JD006594, 2006.

van der A, R. J., Mijling, B., Ding, J., Koukouli, M. E., Liu, F., Li, Q., Mao, H., and Theys, N.: Cleaning up the air: effectiveness of air quality policy for SO_2 and NO_x emissions in China, Atmos. Chem. Phys., 17, 1775-1789, https://doi.org/10.5194/acp-17-1775-2017, 2017.

van Loon, M., Builtjes, P. J. H., and Segers, A. J.: Data assimilation of ozone in the atmospheric transport chemistry model LOTOS, Environ. Model. Softw., 15, 603–609, 2000.

Wang, Z., Li, J., Wang, Z., Yang, W., Tang, X., Ge, B., Yan, P., Zhu, L., Chen, X., and Chen, H.: Modeling study of regional severe hazes over mid-eastern China in January 2013 and its implications on pollution prevention and control, Sci.China-Earth Sci., 57, 3–13, 2014.

Whitaker, J. S., and Hamill, T. M.: Ensemble data assimilation without perturbed observations, Mon. Weather Rev.,

130, 1913–1924, 2002.

Wild, O., Zhu, X., and Prather, M. J.: Fast-j: Accurate simulation of in- and below-cloud photolysis in tropospheric chemical models, J. Atmos. Chem., 37, 245–282, doi:10.1023/A:1006415919030, 2000.

Xie, Y., Ding, A., Nie, W., Mao, H., Qi, X., Huang, X., Xu, Z., Kerminen, V.-M., Petäjä, T., Chi, X., Virkkula, A., Boy, M., Xue, L., Guo, J., Sun, J., Yang, X., Kulmala, M., and Fu, C.: Enhanced sulfate formation by nitrogen dioxide: Implications from in situ observations at the SORPES station, J. Geophys. Res. – Atmos., 120, 24, 12679-12694, 2015.

Yang, Y. R., Liu, X. G., Qu, Y., An, J. L., Jiang, R., Zhang, Y. H., Sun, Y. L., Wu, Z. J., Zhang, F., Xu, W. Q., and Ma, Q. X.: Characteristics and formation mechanism of continuous hazes in China: a case study during the autumn of 2014 in the North China Plain, Atmos. Chem. Phys., 15, 8165–8178, doi:10.5194/acp-15-8165-2015, 2015.

Yumimoto, K., Uno, I., Sugimoto, N., Shimizu, A., Liu, Z., and Winker, D. M.: Adjoint inversion modeling of Asian dust emission using lidar observations, Atmos. Chem. Phys., 8, 2869-2884, doi:10.5194/acp-8-2869-2008, 2008.

Yumimoto, K., Uno, I., Sugimoto, N., Shimizu, A., and Satake, S.: Adjoint inverse modeling of dust emission and transport over East Asia, Geophys. Res. Lett., 34, L00806, doi:10.029/2006GL028551, 2007.

Zhang, Q., Streets, D. G., Carmichael, G. R., He, K. B., Huo, H., Kannari, A., Klimont, Z., Park, I. S., Reddy, S., Fu, J. S., Chen, D., Duan, L., Lei, Y., Wang, L. T., and Yao, Z. L.: Asian emissions in 2006 for the NASA INTEX-B mission, Atmos. Chem. Phys., 9, 5131-5153, doi:10.5194/acp-9-5131-2009, 2009.

Zhang, R., Wang, G., Guo, S., Zamora, M. L., Ying, Q., Lin, Y., Wang, W., Hu, M., and Wang, Y.: Formation of Urban Fine Particulate Matter, Chem. Rev., 115, 3803–3855, doi:10.1021/acs.chemrev.5b00067, 2015a.

Zhang, L., Shao, J. Y., Lu, X., Zhao, Y. H., Hu, Y. Y., Henze, D. K., et al.: Sources and processes affecting fine particulate matter pollution over North China: An adjoint analysis of the Beijing APEC period. Environmental Science & Technology, 50(16), 8731–8740. https://doi.org/10.1021/acs.est.6b03010, 2016.

Zhang, L., Li, Q., Wang, T., Ahmadov, R., Zhang, Q., Li, M., and Lv, M.: Combined impacts of nitrous acid and nitryl chloride on lower-tropospheric ozone: new module development in WRF-Chem and application to China, Atmos. Chem. Phys., 17, 9733-9750, https://doi.org/10.5194/acp-17-9733-2017, 2017.

Zhao, X. J., Zhao, P. S., Xu, J., Meng,,W., Pu,W.W., Dong, F., He, D., and Shi, Q. F.: Analysis of a winter regional haze event and its formation mechanism in the North China Plain, Atmos. Chem. Phys., 13, 5685–5696, doi:10.5194/acp-13-5685-2013, 2013.

Zheng, B., Zhang, Q., Zhang, Y., He, K. B., Wang, K., Zheng, G. J., Duan, F. K., Ma, Y. L., and Kimoto, T.: Heterogeneous chemistry: a mechanism missing in current models to explain secondary inorganic aerosol formation during the January 2013 haze episode in North China, Atmos.Chem.Phys., 15, 2031-2049, 10.5194/acp-15-2031-2015, 2015.

List of Figures and Tables

Table 1. WRF-Chem model configurations in this study.

Table 2. State vectors in the data assimilation system.

Figure 1. The model domain (left) and the North China Plain (right). Black dots are the observational sites used for assimilation, and red stars are the observational sites used for validation. The green frame marks the Beijing–Tianjin–Hebei region.

809 Figure 2. Time series of prior ensemble mean RMSE (blue line) and total spread (black
810 line) for $PM_{2.5}$, PM_{10}, SO_2, NO_2, CO and O_3 concentrations aggregated over all
811 observations over the Beijing–Tianjin–Hebei region. Units for all these variables are
812 $\mu g \cdot m^{-3}$.

813 Figure 3. Time series of the area-averaged ensemble spread for the emission scaling

814 factors over the Beijing–Tianjin–Hebei region.

815 Figure 4. Time series of the hourly pollutant concentrations in the Beijing–Tianjin–
816 Hebei (BTH) region obtained from observations (red line), the control run (black line),
817 the analysis (pink line), the first-day forecast from fcICsEs (fcICsEs24, blue line), and
818 the first-day forecast from fcICs (fcICs24, blue line). The observations were obtained
819 from the 47 independent sites in the BTH region. The modelled time series were
820 interpolated to the 47 independent sites using the spatial bilinear interpolator method.
821 The shaded backgrounds indicate the distribution of the observations, where the top
822 edge represented the 90th percentile and the bottom edge the 10th percentile. Units:
823 $\mu g \cdot m^{-3}$.

824 Table 3. Comparison with observations of the surface $PM_{2.5}$ mass concentrations in the
825 Beijing–Tianjin–Hebei region from the control experiment, the assimilation experiment,
826 and the first-day forecast, over all analysis times from 6 to 16 October 2014. Units:
827 $\mu g \cdot m^{-3}$.

828 Figure 5. Bias of surface $PM_{2.5}$, PM_{10}, SO_2, NO_2, CO and O_3 as a function of forecast
829 range calculated against all the independent observations over the Beijing–Tianjin–
830 Hebei region shown in Figure 1. The 72-h forecasts were performed at each 0000 UTC
831 from 6 to 14 October 2014 and the statistics were computed from 6 to 14 October. Units:
832 $\mu g \cdot m^{-3}$.

833 Figure 6. As in Figure 5 but for RMSE. Units: $\mu g \cdot m^{-3}$.

834 Figure 7. Normalized RMSE (assimilation divided by control) for fcICsEs and fcICs
835 for $PM_{2.5}$, PM_{10}, SO_2 and CO.

836 Figure 8. Spatial distribution of the prescribed emissions (top panels) of $PM_{2.5}$ (left), PM_{10} (middle),
837 and NH_3 (right) and the corresponding time-averaged differences between the ensemble mean
838 analysis and the prescribed values at the lowest model level averaged over all hours from 6 to
839 16 October 2014 in the NCP region. Units for $PM_{2.5}$ and PM_{10} emissions: $\mu g \cdot m^{-2} \cdot s^{-1}$; and
840 for NH_3 emissions: $mol \cdot km^{-2} \cdot hr^{-1}$.

841 Figure 9. As in Figure 8 but for SO_2 (left), NO (middle), and CO (right). Units for SO_2, NO
842 and CO emissions: $mol \cdot km^{-2} \cdot hr^{-1}$.

843 Figure 10. Hourly area-averaged time series extracted from the analyzed emission
844 scaling factors (black line), the forecast emission scaling factors (green dashed line),
845 the analyzed emissions (blue line), and the prescribed emissions (blue dashed line) in
846 the Beijing–Tianjin–Hebei region. Units for $PM_{2.5}$ and PM_{10} emissions: $\mu g \cdot m^{-2} \cdot s^{-1}$; and
847 for NH_3, SO_2, NO and CO emissions: $mol \cdot km^{-2} \cdot hr^{-1}$.

848

849

850 Table 1. WRF-Chem model configurations in this study.

Parameterization	WRF-Chem Option
Aerosol scheme	Goddard Chemistry Aerosol Radiation and Transport (Chin et al., 2000, 2002)
Photolysis scheme	Fast-J (Wild et al., 2000)
Gas-phase chemistry	Regional Atmospheric Chemistry Mechanism (Stockwell et al., 1997)
Microphysics	the WRF single-moment 5 class scheme
Longwave radiation	Rapid Radiative Transfer Model longwave scheme (Mlawer et al., 1997)
shortwave radiation	Goddard shortwave radiation scheme (Chou and Suarez, 1994)
Planetary boundary layer	Yonsei University boundary layer scheme (Hong et al., 2006)
cumulus parameterization	Grell-3D scheme
Land-surface model	NOAH (Chen and Dudhia, 2001)
Dust and sea salt emissions	Goddard Chemistry Aerosol Radiation and Transport (Chin et al., 2002)

851

852

853

854

Table 2. State vectors in the data assimilation system.

Observations	PM$_{2.5}$	PM$_{10-2.5}$	SO$_2$	NO$_2$	CO	O$_3$
Mass concentration	P$_{25}$, S, OC$_1$, OC$_2$ BC$_1$, BC$_2$, D$_1$, D$_2$, S$_1$, S$_2$	P$_{10}$, D$_3$, D$_4$, D$_5$ S$_3$, S$_4$,	SO$_2$	NO, NO$_2$	CO	O$_3$
Scaling factors	$\lambda_{PM2.5}$, λ_{NH3}	λ_{PM10}	λ_{SO2}	λ_{NO}	λ_{CO}	—
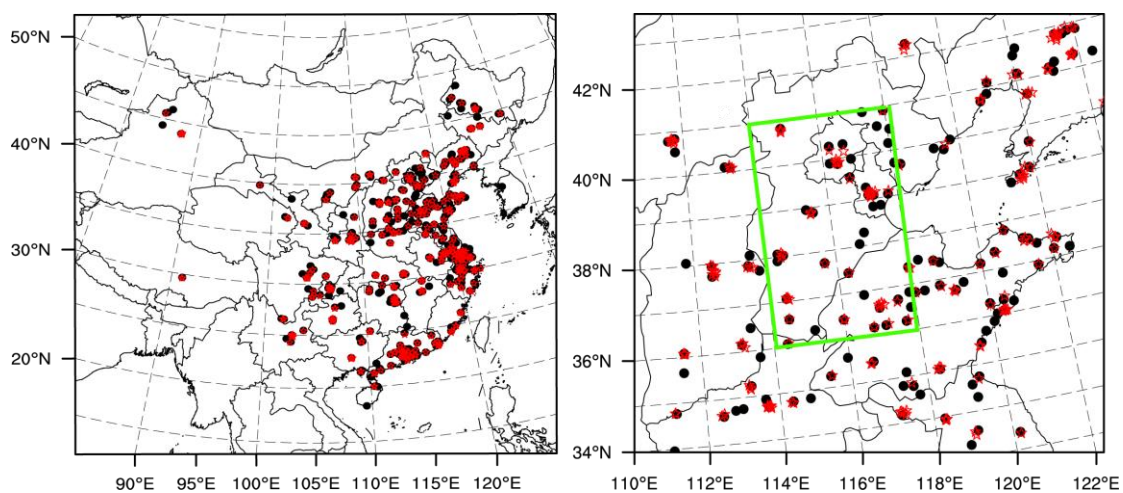
855

856

859   Figure 1. The model domain (left) and the North China Plain (right). Black dots are

860   the observational sites used for assimilation, and red stars are the observational sites

861   used for validation. The green frame marks the Beijing–Tianjin–Hebei region.

862

863

864

865   Figure 2. Time series of prior ensemble mean RMSE (blue line) and total spread
866 (black line) for $PM_{2.5}$, PM_{10}, SO_2, NO_2, CO and O_3 concentrations aggregated over all
867   observations over the Beijing–Tianjin–Hebei region. Units for all these variables are
868                                       $\mu g \cdot m^{-3}$.

869

870

871
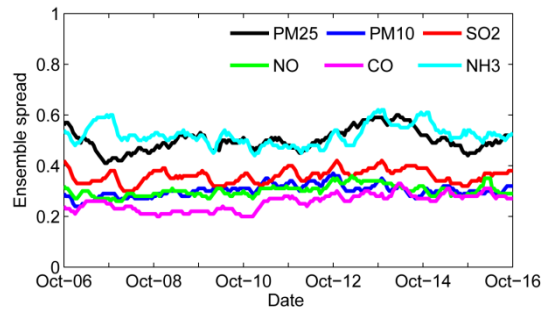
872

Figure 3. Time series of the area-averaged ensemble spread for the emission scaling

factors over the Beijing–Tianjin–Hebei region.

875
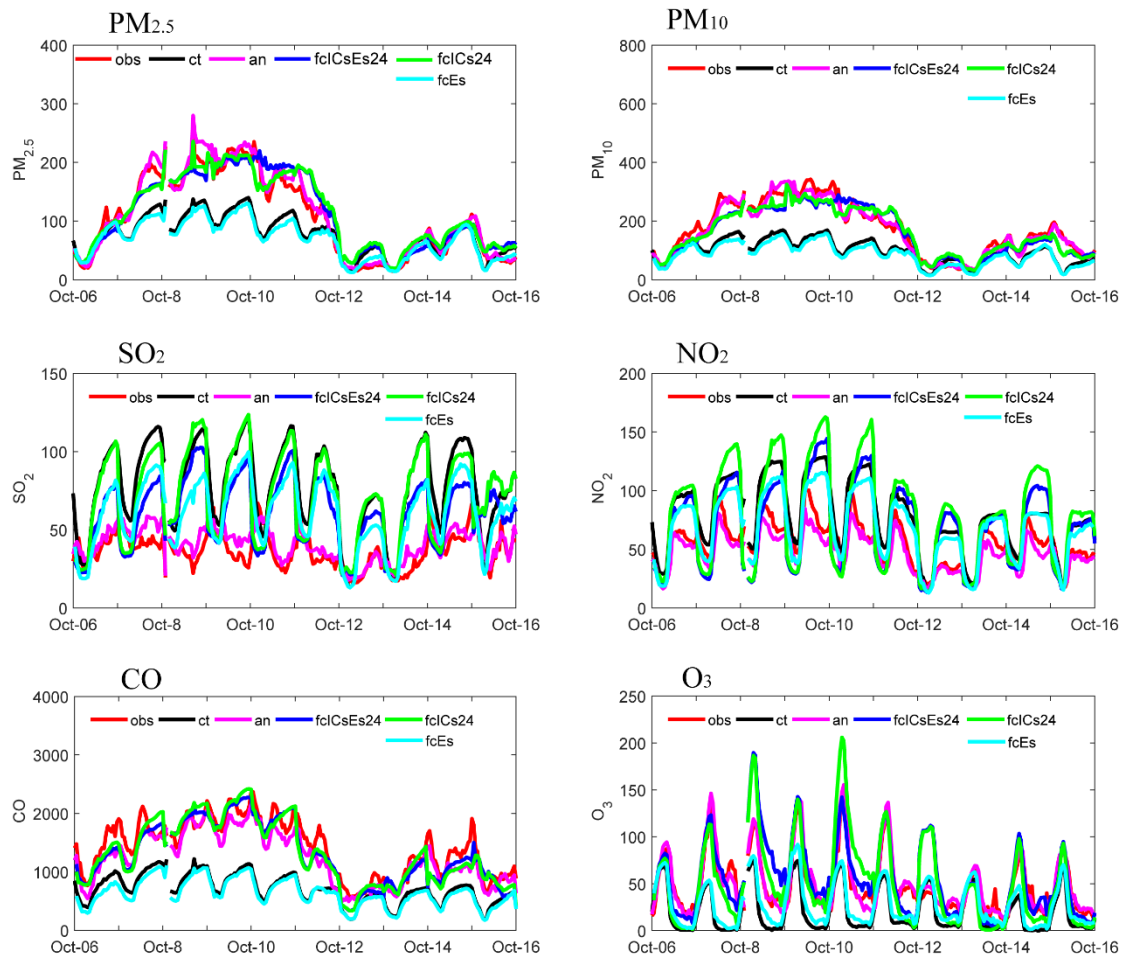
Figure 4. Time series of the hourly pollutant concentrations in the Beijing–Tianjin–Hebei (BTH) region obtained from observations (referred to as "obs", red line), the control run (referred to as "ct", black line), the analysis (referred to as "an", pink line), the first-day forecast from fcICsEs (referred to as "fcICsEs24", blue line), the first-day forecast from fcICs (referred to as "fcICs24", blue line), and the simulation only using the optimized emissions (referred to as "fcEs", cyan line). The observations were obtained from the 47 independent sites in the BTH region. The modelled time series were interpolated to the 47 independent sites using the spatial bilinear interpolator method. Units: $\mu g \cdot m^{-3}$.

Table 3. Comparison with observations of the surface PM$_{2.5}$ mass concentrations in the Beijing–Tianjin–Hebei region from the control experiment, the assimilation experiment, and the first-day forecast, over all analysis times from 6 to 16 October 2014. Units: μg·m^{-3}.

Species	Experiment	Mean observed value	Mean simulated value	BIAS	RMSE	CORR
PM$_{2.5}$	Control		80.7	−34.1	92.1	0.740
	Analysis	114.8	119.9	5.1	51.5	0.891
	fcICsEs24		121.2	6.5	77.8	0.736
	fcICs24		123.1	8.3	75.1	0.748
PM$_{10}$	Control		96.9	−77.7	134.6	0.691
	Analysis	174.6	169.0	−5.6	63.4	0.890
	fcICsEs24		162.7	−11.9	98.7	0.716
	fcICs24		164.3	−10.3	95.9	0.726
SO$_2$	Control		81.1	48.1	66.6	0.088
	Analysis	33.0	41.1	8.1	27.9	0.540
	fcICsEs24		62.0	29.0	51.2	0.120
	fcICs24		75.7	42.7	65.8	0.038
NO$_2$	Control		78.8	22.4	39.7	0.545
	Analysis	56.4	48.0	−8.3	31.7	0.557
	fcICsEs24		71.8	15.4	46.2	0.408
	fcICs24		82.8	26.4	55.5	0.414
CO	Control		752.3	−565.7	962.7	0.354
	Analysis	1318.0	1157.5	−160.4	618.9	0.705
	fcICsEs24		1418.4	100.4	805.1	0.476
	fcICs24		1448.2	130.2	838.2	0.439
O$_3$	Control		26.5	−31.0	50.8	0.463
	Analysis	57.5	59.6	2.1	31.1	0.753
	fcICsEs24		63.5	6.0	49.0	0.460

	fcICs24		58.98	1.5	50.5	0.478

892

893
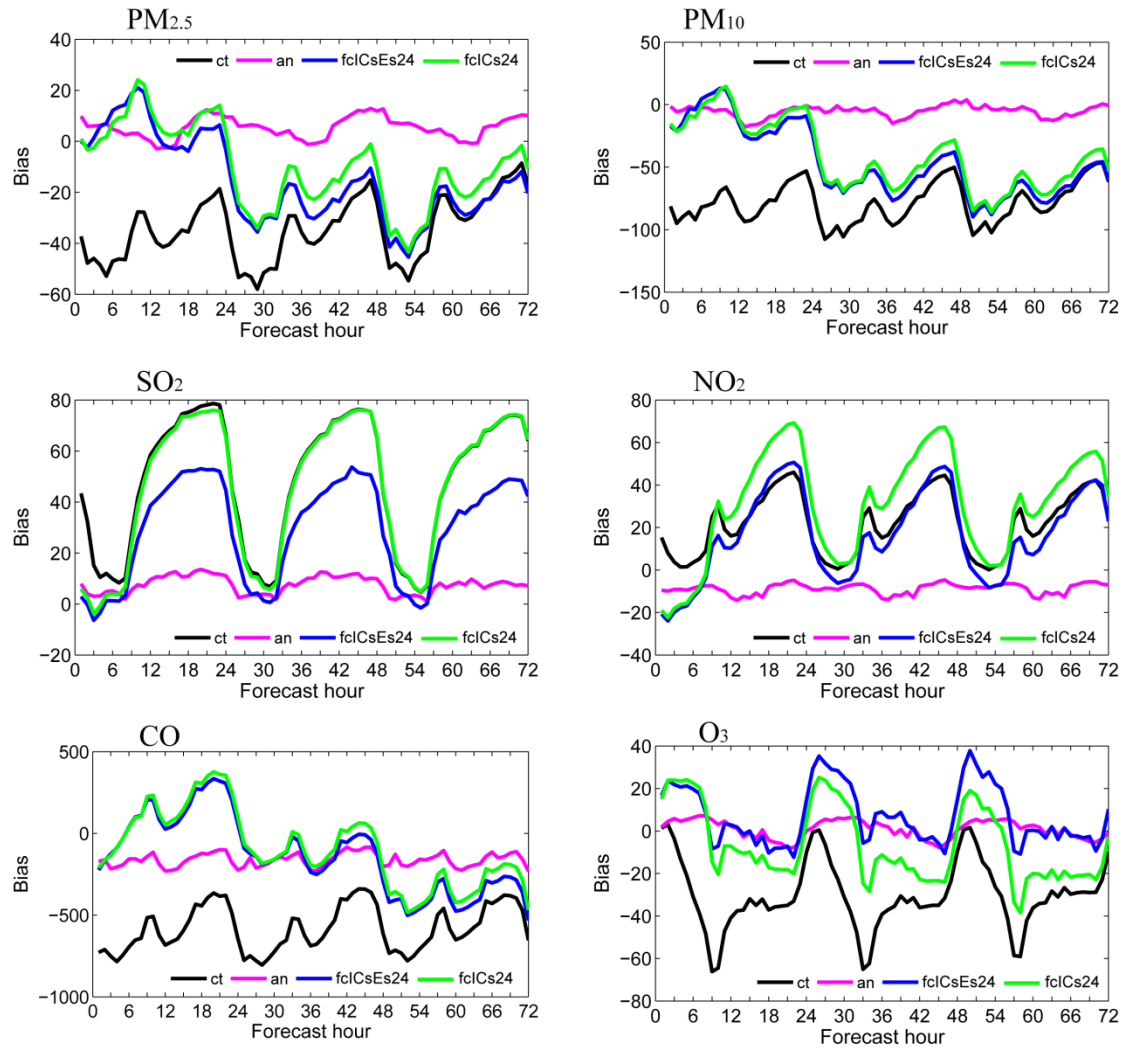
894

895 Figure 5. Bias of surface PM2.5, PM10, SO2, NO2, CO and O3 as a function of forecast
896 range calculated against all the independent observations over the Beijing–Tianjin–
897 Hebei region shown in Figure 1. The 72-h forecasts were performed at each 0000
898 UTC from 6 to 14 October 2014 and the statistics were computed from 6 to 14
899 October. Units: $\mu g \cdot m^{-3}$.

900

901

902
903 Figure 6. As in Figure 5 but for RMSE. Units: μg·m^{-3}.
904
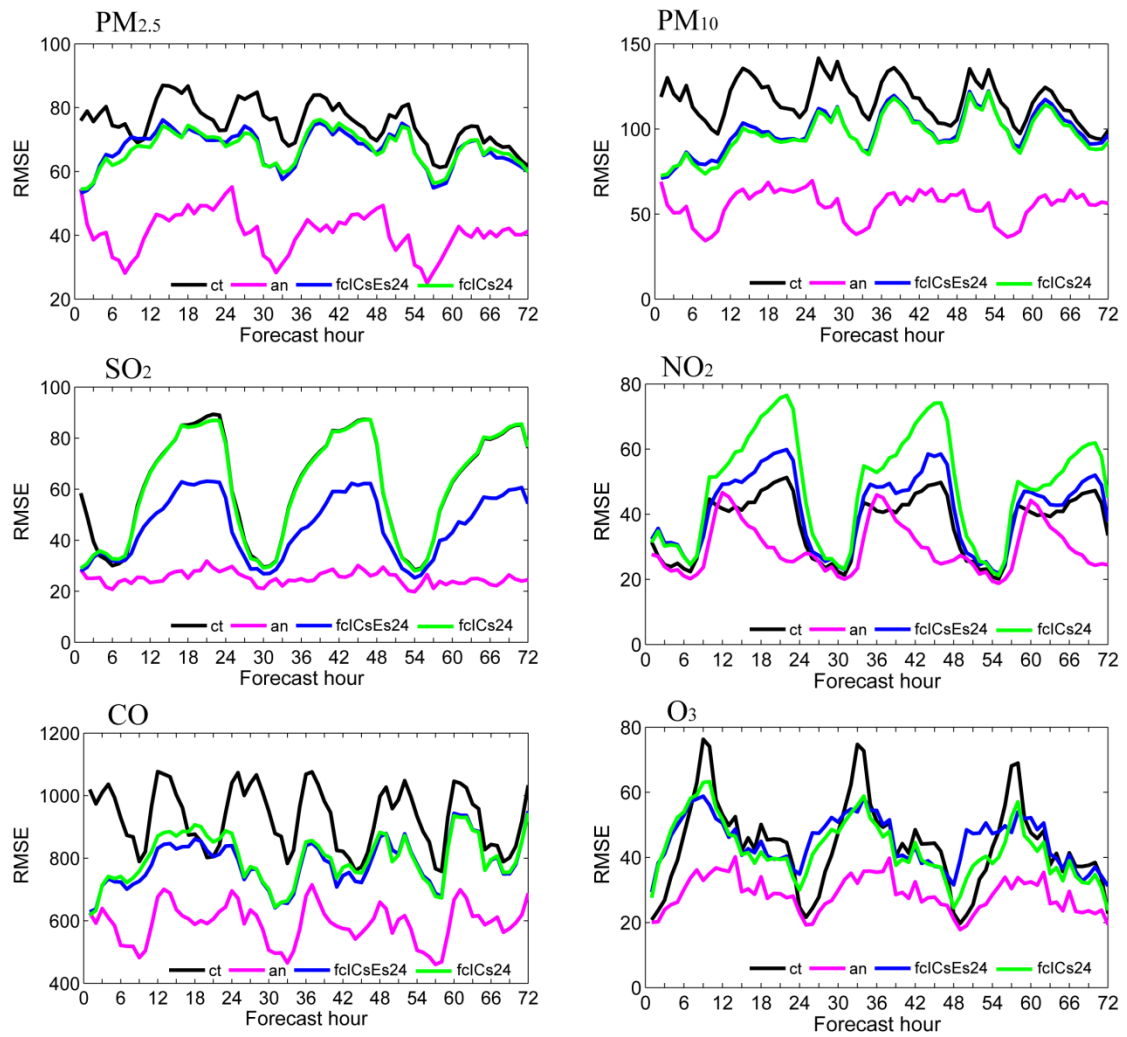
905
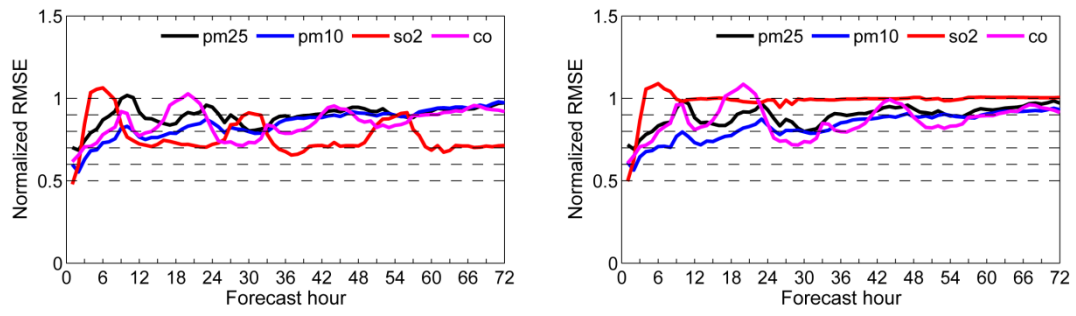
906

907 Figure 7. Normalized RMSE (assimilation divided by control) for fcICsEs and fcICs
908 for $PM_{2.5}$, PM_{10}, SO_2 and CO.

909
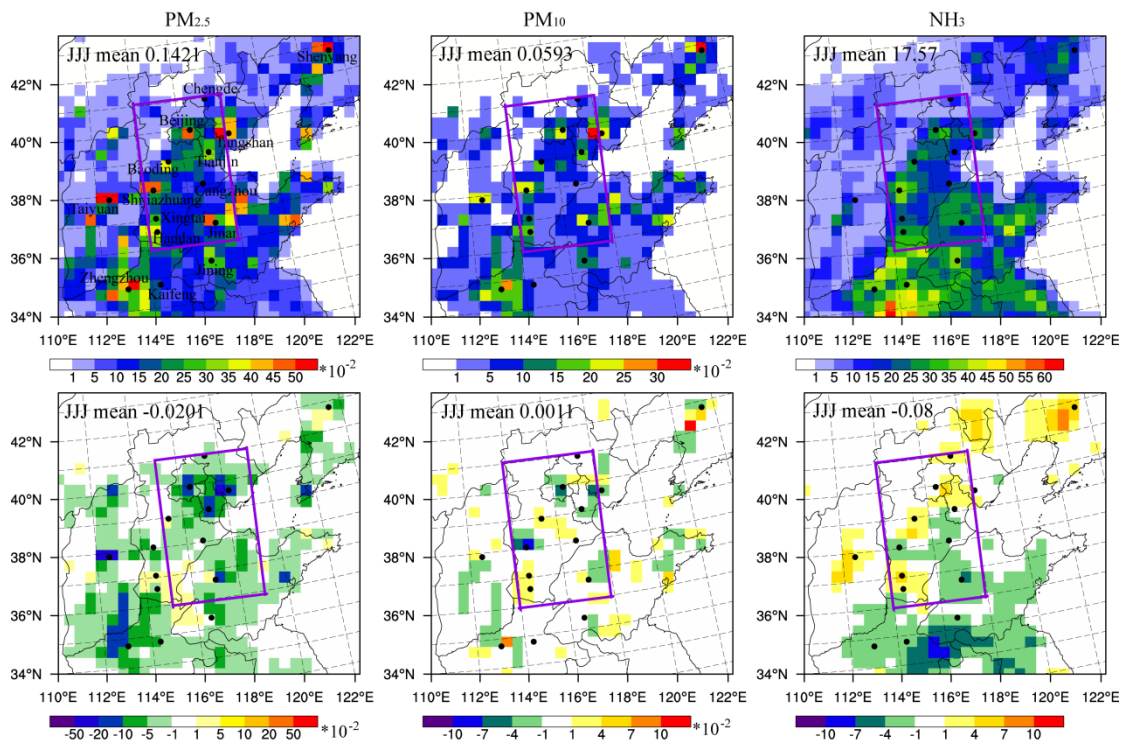
912 Figure 8. Spatial distribution of the prescribed emissions (top panels) of PM$_{2.5}$ (left), PM$_{10}$
913 (middle), and NH$_3$ (right) and the corresponding time-averaged differences between the ensemble
914 mean analysis and the prescribed values at the lowest model level averaged over all hours
915 from 6 to 16 October 2014 in the NCP region. Units for PM$_{2.5}$ and PM$_{10}$ emissions:
916 μg·m^{-2}·s^{-1}; and for NH$_3$ emissions: mol·km^{-2}·hr^{-1}.

917

918

919
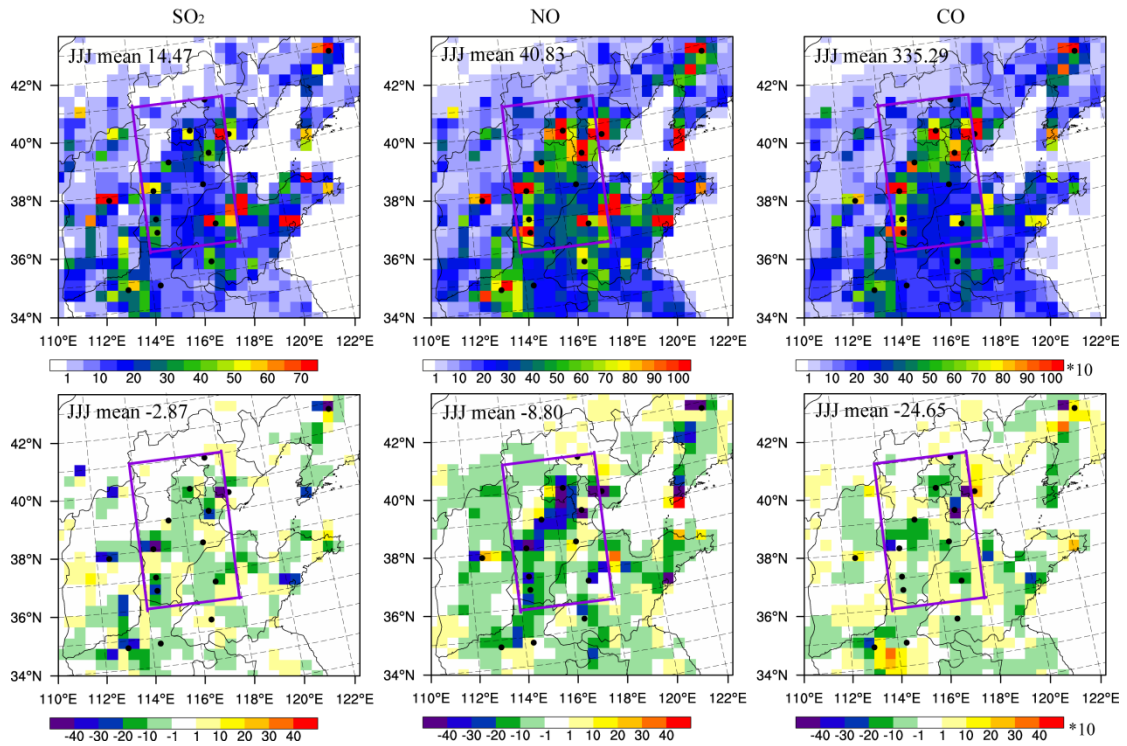
Figure 9. As in Figure 8 but for SO$_2$ (left), NO (middle), and CO (right). Units for SO$_2$, NO and CO emissions: mol·km^{-2}·hr^{-1}.
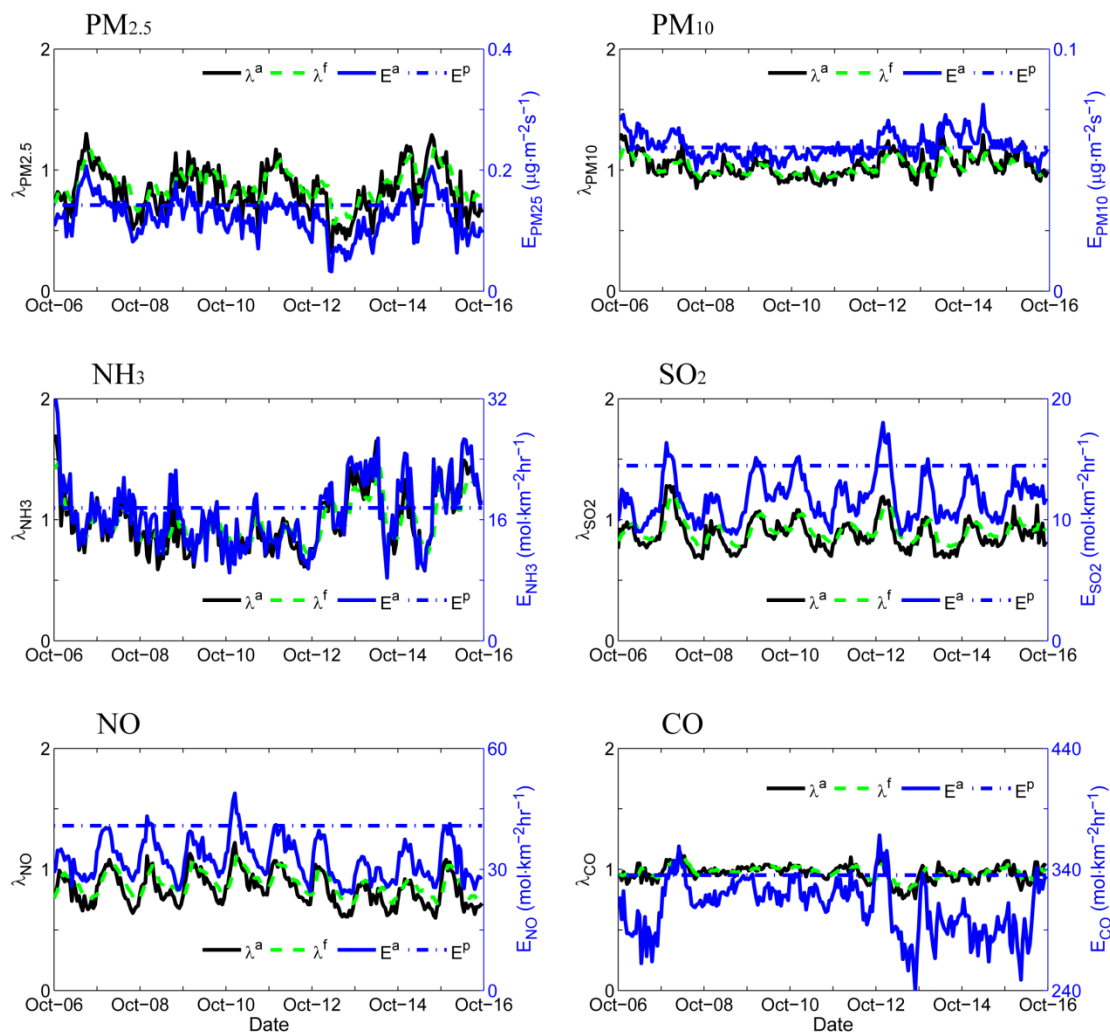
922

923

924

Figure 10. Hourly area-averaged time series extracted from the analyzed emission scaling factors (black line), the forecast emission scaling factors (green dashed line), the analyzed emissions (blue line), and the prescribed emissions (blue dashed line) in the Beijing–Tianjin–Hebei region. Units for PM$_{2.5}$ and PM$_{10}$ emissions: μg·m^{-2}·s^{-1}; and for NH$_3$, SO$_2$, NO and CO emissions: mol·km^{-2}·hr^{-1}.

930

931
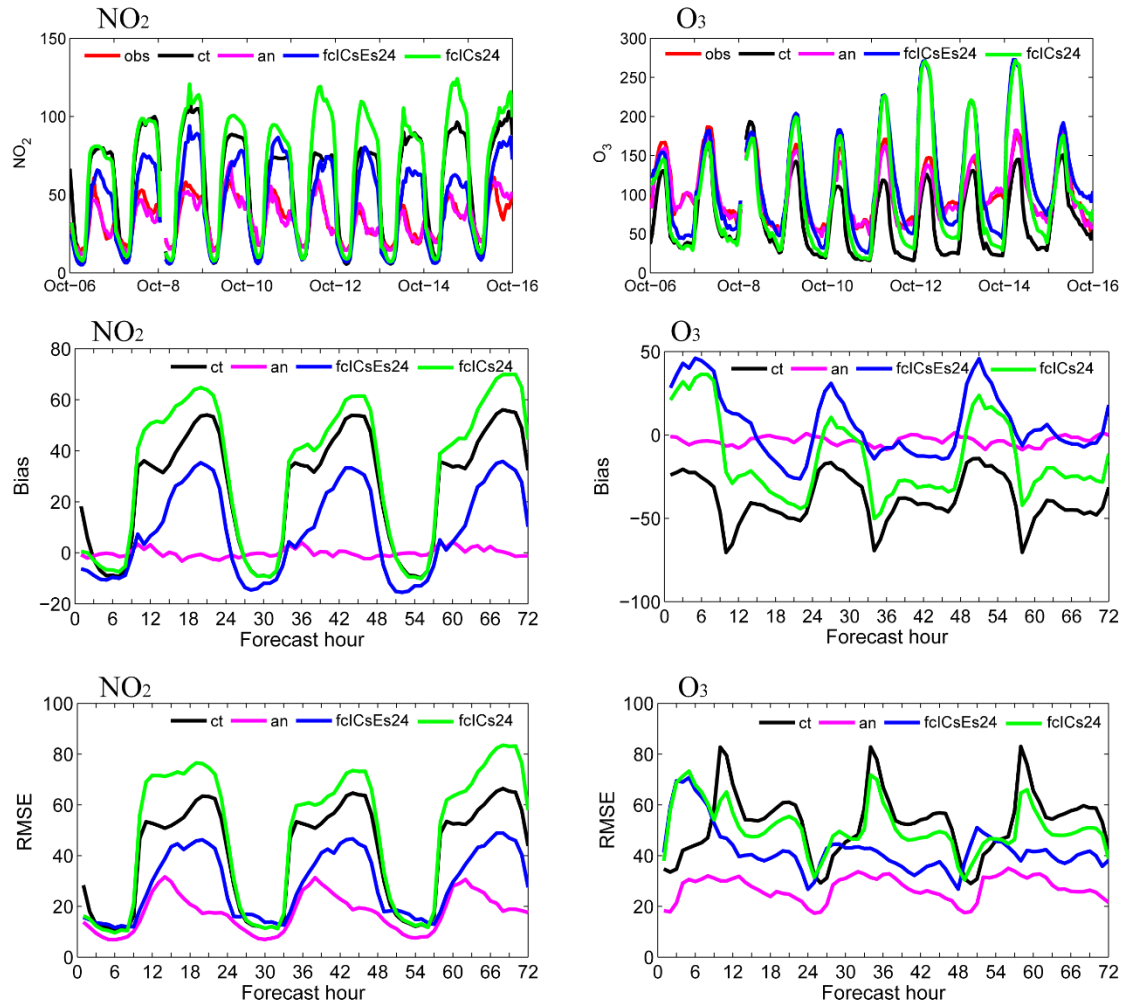
Figure 11. NO₂ and O₃ time series of the hourly pollutant concentrations in the Pearl
River Delta region (PRD, 21°–24°N, 112.5°–115°E) obtained from observations
(referred to as "obs", red line), the control run (referred to as "ct", black line), the
analysis (referred to as "an", pink line), the first-day forecast from fcICsEs (referred
to as "fcICs24", blue line), and the first-day forecast from fcICs (referred to as
"fcICs24", blue line). The bias and RMSEs of surface NO₂ and O₃ as a function of
forecast range calculated against all the independent observations (34 sites) over the
PRD region. Units: μg·m⁻³.